A Poly-ADP-Ribose Trigger Releases the Auto-Inhibition of a Chromatin Remodeling Oncogene

Singh, H.R.; Nardozza, A.P.; Moller, I.R.; Knobloch, G.; Kistemaker, H.A.V.; Hassler, M.; ... ; Ladurner, A.G.

Article

Molecular Cell

A Poly-ADP-Ribose Trigger Releases the Auto-Inhibition of a Chromatin Remodeling Oncogene

Graphical Abstract

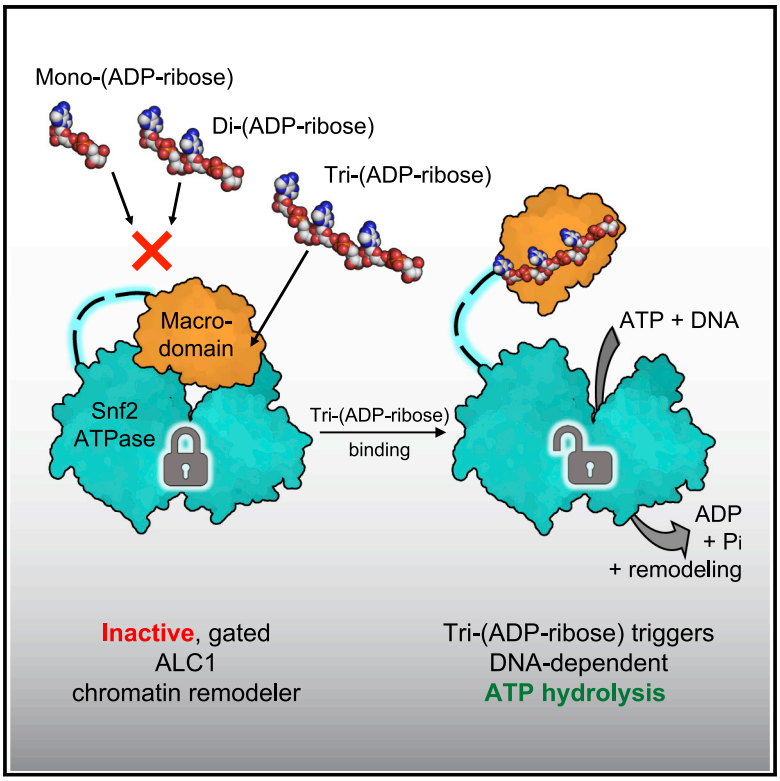

Highlights

- The ALC1 macrodomain mediates auto-inhibition of the remodeler's ATPase activity
- PARP1 hyper-activation suppresses the inhibitory protein-protein interaction
- Tri-ADP-ribose promotes an ungated ALC1 conformation and triggers ATPase activity
- Somatic cancer mutations disrupt ALC1's auto-inhibitory mechanism in living cells

Authors

Hari R. Singh, Aurelio P. Nardozza, Ingvar R. Möller, ..., Gyula Timinszky, Kasper D. Rand, Andreas G. Ladurner

Correspondence

kasper.rand@sund.ku.dk (K.D.R.), andreas.ladurner@bmc.med.lmu.de (A.G.L.)

In Brief

The activity of the human oncogene and chromatin remodeler ALC1/CHD1L is strictly regulated by PARP1 activation. Singh et al. reveal how oligomers of ADP-ribose trigger the activation of ALC1 from an auto-inhibited state and identify cancer mutations that disrupt the NAD^+-metabolite-regulated allosteric mechanism.

Singh et al., 2017, Molecular Cell *68*, 860–871
December 7, 2017
https://doi.org/10.1016/j.molcel.2017.11.019

CellPress

CellPress

Molecular Cell
Article

A Poly-ADP-Ribose Trigger Releases the Auto-Inhibition of a Chromatin Remodeling Oncogene

Hari R. Singh,[1] Aurelio P. Nardozza,[1,11] Ingvar R. Möller,[2,11] Gunnar Knobloch,[1,11] Hans A.V. Kistemaker,[3] Markus Hassler,[1,4] Nadine Harrer,[1] Charlotte Blessing,[1] Sebastian Eustermann,[5] Christiane Kotthoff,[1] Sébastien Huet,[6,7] Felix Mueller-Planitz,[1] Dmitri V. Filippov,[3] Gyula Timinszky,[1] Kasper D. Rand,[2,*] and Andreas G. Ladurner[1,8,9,10,*]

[1]Biomedical Center Munich, Faculty of Medicine, Ludwig-Maximilians-Universität München, Großhaderner Street 9, 82152 Planegg-Martinsried, Germany

[2]Department of Pharmacy, Faculty of Health and Medical Sciences, University of Copenhagen, Universitetsparken 2, 2100 Copenhagen, Denmark

[3]Leiden Institute of Chemistry, Department of Bio-organic Synthesis, Leiden University, Einsteinweg 55, 2333 CC Leiden, the Netherlands

[4]Cell Biology and Biophysics Unit, European Molecular Biology Laboratory (EMBL), Meyerhofstraße 1, 69117 Heidelberg, Germany

[5]Gene Center and Department of Biochemistry, Ludwig-Maximilians-Universität München, Feodor-Lynen Street 25, 81377 Munich, Germany

[6]CNRS, UMR 6290, Institut Génétique et Développement de Rennes, 35043 Rennes, France

[7]Université de Rennes 1, Structure Fédérative de Recherche Biosit, 35043 Rennes, France

[8]Center for Integrated Protein Science Munich, Ludwig-Maximilians-Universität München, Butenandt Street 13, 81377 Munich, Germany

[9]Munich Cluster for Systems Neurology, Ludwig-Maximilians-Universität München, Feodor Lynen Street 17, 81377 Munich, Germany

[10]Lead Contact

[11]These authors contributed equally

*Correspondence: kasper.rand@sund.ku.dk (K.D.R.), andreas.ladurner@bmc.med.lmu.de (A.G.L.)

https://doi.org/10.1016/j.molcel.2017.11.019

SUMMARY

DNA damage triggers chromatin remodeling by mechanisms that are poorly understood. The oncogene and chromatin remodeler ALC1/CHD1L massively decompacts chromatin *in vivo* yet is inactive prior to DNA-damage-mediated PARP1 induction. We show that the interaction of the ALC1 macrodomain with the ATPase module mediates auto-inhibition. PARP1 activation suppresses this inhibitory interaction. Crucially, release from auto-inhibition requires a poly-ADP-ribose (PAR) binding macrodomain. We identify tri-ADP-ribose as a potent PAR-mimic and synthetic allosteric effector that abrogates ATPase-macrodomain interactions, promotes an ungated conformation, and activates the remodeler's ATPase. ALC1 fragments lacking the regulatory macrodomain relax chromatin *in vivo* without requiring PARP1 activation. Further, the ATPase restricts the macrodomain's interaction with PARP1 under non-DNA damage conditions. Somatic cancer mutants disrupt ALC1's auto-inhibition and activate chromatin remodeling. Our data show that the NAD$^+$-metabolite and nucleic acid PAR triggers ALC1 to drive chromatin relaxation. Modular allostery in this oncogene tightly controls its robust, DNA-damage-dependent activation.

INTRODUCTION

Chromatin structure safeguards the integrity of our genome. Distinct families of chromatin remodeling enzymes establish and maintain chromatin structure, for example by facilitating the binding of transcription factors to functional DNA elements or assisting the repair machinery upon DNA damage. Key to controlling the activity of these ATPases are chromatin targeting mechanisms and regulatory interactions (Dann et al., 2017). Such mechanisms help ensure that remodelers are only active where and when needed. While the mechanisms through which the Chd1 and ISWI remodelers are regulated by nucleosomes have been explored (Clapier and Cairns, 2012; Hauk et al., 2010; Ludwigsen et al., 2017; Yan et al., 2016), less is known about how DNA damage triggers the activity of remodelers such as the PARP1-dependent ALC1 (Ahel et al., 2009; Gottschalk et al., 2012; 2009), which massively decompacts chromatin upon DNA damage (Movie S1; Sellou et al., 2016). Considering *ALC1*'s validated roles as an oncogene (*ALC1* is amplified in several cancers and promotes metastases, proliferation, and pluripotency; Chen et al., 2010; Jiang et al., 2015; Kulkarni et al., 2013; Ma et al., 2008), understanding how PAR triggers ALC1 activity would advance our molecular understanding of how DNA damage impacts our genome, shed light on how a NAD$^+$ metabolite and nucleic acid triggers the activation of an oncogene, and reveal approaches that might allow us to target ALC1 therapeutically.

Single-strand DNA breaks rapidly induce the activity of PARP1, PARP2, and PARP3, enzymes that use NAD$^+$ to ADP-ribosylate chromatin and other cellular targets (Carter-O'Connell

et al., 2016; Gibson et al., 2016; Grundy et al., 2016). The clinical promise of PARP1 inhibitors in cancer therapy (Lord and Ashworth, 2017) and the identification of domains that recognize ADP-ribosylated proteins, including ADP-ribose binding macrodomains (Karras et al., 2005; Kustatscher et al., 2005), has rekindled interest in NAD^+ signaling (Cambronne et al., 2016; Kim et al., 2004; Petesch and Lis, 2012; Tulin and Spradling, 2003). While cellular mono-ADP-ribosylation, catalyzed by related PARP enzymes, is thought to act as a reversible, regulatory post-translational modification (PTM) (Jankevicius et al., 2013; Rosenthal et al., 2013; Sharifi et al., 2013), the tightly regulated synthesis of PAR by PARP1 and PARP2 profoundly alters nuclear organization and cellular homeostasis (Altmeyer et al., 2015; Asher et al., 2010; Bai et al., 2011a; 2011b; Wright et al., 2016).

PAR is a nucleic acid with important roles in the stress response to DNA damage. It is as an abundant, transient polymeric anion that can promote phase separation (Altmeyer et al., 2015; Asher et al., 2010; Bai et al., 2011a, 2011b; Wright et al., 2016). Sites of high PARP1 activity *in vivo* recruit ATP-dependent remodelers, including ALC1 (Amplified in Liver Cancer 1; also known as CHD1L), CHD2, CHD4, SMARCA5/SNF2H, and *Drosophila* Mi-2 (Chou et al., 2010; Murawska et al., 2011; Polo et al., 2010; Smeenk et al., 2013). Remodelers such as ALC1 and CHD2 mediate chromatin relaxation through unknown mechanisms at the site of DNA damage (Luijsterburg et al., 2016; Sellou et al., 2016). These are some of the earliest, PARP-dependent changes in chromatin structure upon DNA damage (Kruhlak et al., 2006; Poirier et al., 1982; Strickfaden et al., 2016).

Others and we have shown that ALC1 recruits to DNA damage sites upon PARP1 activation. Recruitment and PAR binding requires its C-terminal, PAR-binding macrodomain module (Ahel et al., 2009; Gottschalk et al., 2009, 2012; Jiang et al., 2015). Interestingly, its ATPase and nucleosome-remodeling activities depend on PARP1 activation. *In vitro* assays reveal that PARylated PARP1 promotes ALC1-dependent nucleosome sliding (Ahel et al., 2009; Gottschalk et al., 2009, 2012). Key to ALC1's activity is the ability of its macrodomain to recognize PARylated PARP1. However, what keeps ALC1 inactive prior to PARP1 activation and how the nuclear metabolite and nucleic acid PAR triggers ALC1 activation are not known.

RESULTS

Modular Auto-Inhibition in the Remodeler ALC1

We set out to investigate what suppresses ALC1 remodeler activity when PARP1 is inactive. Unlike most remodelers, endogenous ALC1 does not purify as a multi-subunit complex, and its remodeling activity can be efficiently reconstituted *in vitro* using recombinant protein and DNA, together with PARP1 and NAD^+ (Ahel et al., 2009; Gottschalk et al., 2009, 2012). The enzyme consists of a two-lobed catalytic Snf2-like ATPase domain with homology to ATP-dependent DExx-box helicase (ATPase, Figure 1A), which is connected through a linker region of unknown function to a C-terminal macrodomain (macro), which mediates PARP1 activity-dependent chromatin-targeting (Ahel et al., 2009; Gottschalk et al., 2009, 2012).

To establish whether the ALC1 ATPase domain and macrodomain interact, we generated an ATPase fragment (residues 31–615; "ATPase module") and a fragment containing both linker and C-terminal macrodomain (residues 616–878; "macro module") (Figure 1A). The domain boundaries were identified using limited proteolysis (Figure S1). The recombinant ATPase and macrodomain modules can be expressed individually in *E. coli* and purified to homogeneity. Multiple lines of biochemical evidence show that the two modules form a stable complex. The two fragments interact with each other in pull-down assays (Figure 1B). Size-exclusion chromatography assays reveal the formation of a stoichiometric 1:1 complex (Figure 1C), which elutes with a molecular size (~138 kDa) close to that of the (near) full-length ALC1 construct (residues 31—878; eluting at ~131 kDa; Figure 1D). Thus, ALC1 behaves as a monomer. To determine the affinity of the two ALC1 modules for each other, we employed isothermal titration calorimetry (ITC) assays, which reveal an equilibrium dissociation constant of 96 ± 22 nM (Figure 1E). These results indicate that the ATPase and macrodomain modules of the ALC1 remodeler engage through a tight, intra-molecular interaction.

To test whether this interaction is observed in living cells, we used fluorescence-two-hybrid (F2H) analysis (Zolghadr et al., 2012). Tethering of a fluorescent mCherry-LacI-ALC1 macrodomain bait to an integrated LacO array in U2OS cells enriches the eYFP-tagged ALC1 ATPase prey (Figures 1F and S1), while unrelated macrodomains do not recognize the ALC1 ATPase. We conclude that in the absence of exogenous DNA damage (i.e., when PARP1 has not been induced), the ALC1 modules specifically interact with each other. To rule out the possibility that ALC1 may form dimers, trimers, or other, higher-order complexes through intermolecular domain swapping, we conducted co-immunoprecipitation and F2H assays with full-length ALC1 (Figure S2). Both assays indicate that ALC1 is a monomer *in vivo* (compared to positive controls). Our data suggest that the C-terminal macrodomain of ALC1 packs against one or both of its ATPase lobes in the context of the full-length ALC1 protein, hinting at an intramolecular "gating" function of the ALC1 macrodomain, as described for the unrelated chromodomain of yCHD1 and the NTR domain of ISWI (Hauk et al., 2010; Ludwigsen et al., 2017).

To probe the domain topology of ALC1, we used MS crosslinking. We mapped multiple crosslinks within each of the two ALC1 modules, including between the flexible linker region and the canonical ATPase and macrodomain folds (Figure S1; Table S1). The cross-linking pattern complements well the domain boundaries identified by limited proteolysis (Figure S1). The MS-based crosslinks indicate that the ALC1 hinge contacts the macrodomain and ATPase, confirming our limited proteolysis data. Together, crosslinking and limited proteolysis (Figure S1) hint at a compact arrangement of the ALC1 ATPase and macrodomain modules with respect to each other, consistent with a "gated" structure, which may restrict DNA access to the ATPase motor. We conclude that in the absence of activated PARP1, intramolecular interactions between the macrodomain and ATPase modules establish an auto-inhibited ALC1 conformation.

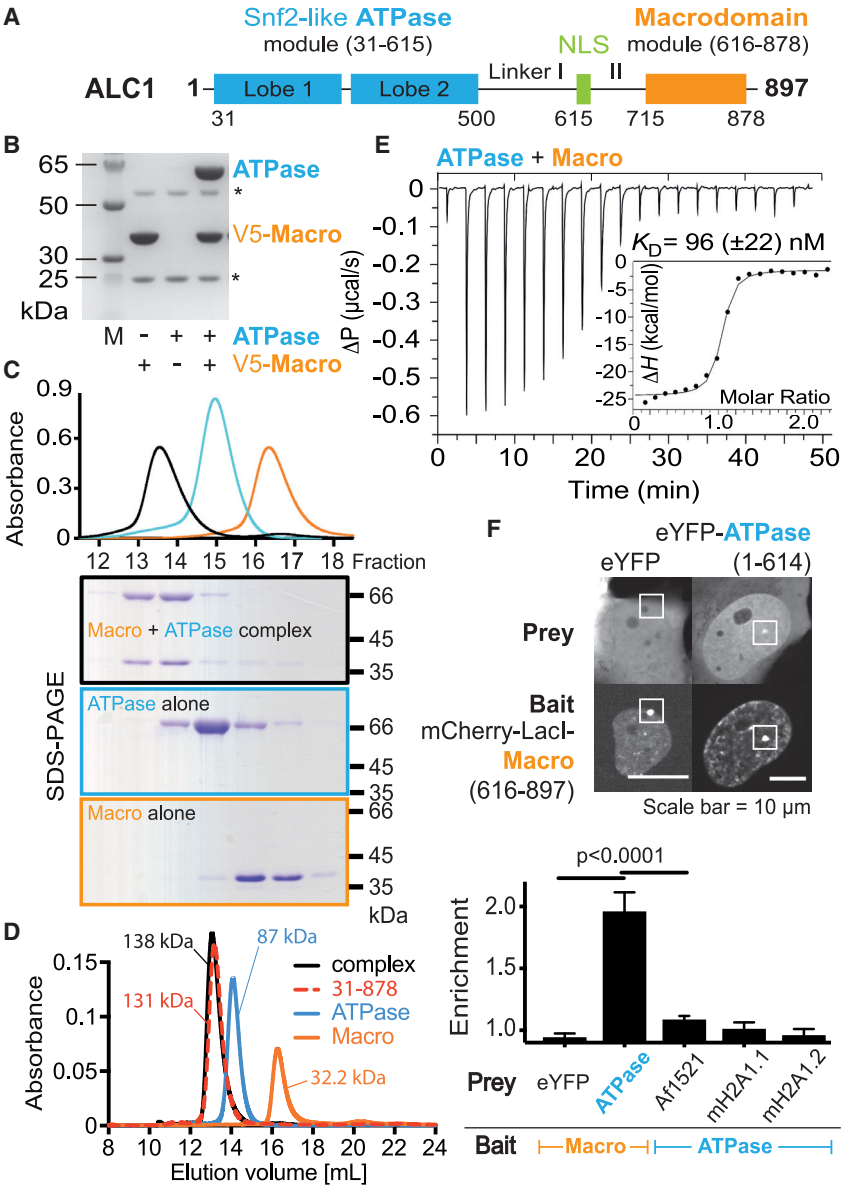

Figure 1. The ALC1 Macrodomain Interacts with the ATPase Module in the Enzyme's Inhibited State

(A) The ALC1 oncogene is composed of two primary modules: an N-terminal Snf2-like ATPase module (residues 31–615) and a C-terminal macrodomain module (616–878). The boundaries were defined using limited proteolysis (Figure S1). NLS, nuclear localization signal.

(B) SDS-PAGE of a V5-based pull-down with recombinant, purified ALC1 macrodomain and ATPase module. The asterisk denotes anti-V5 IgG heavy and light chains.

(C) Size exclusion chromatography (SEC) of recombinant, purified ALC1 macrodomain (residues 636–878,orange), ATPase domain (residues 31–615, cyan), and *in vitro*-reconstituted complex (black), plus SDS-PAGE of the eluted fractions.

(D) Comparison of the elution profiles by gel filtration of the reconstituted ALC1 ATPase–macrodomain complex with purified, near-full-length ALC1 (residues 31–878).

(E) Isothermal titration calorimetry (ITC) assays show that ALC1's two modules bind each other in a high-affinity, exothermic reaction and with 1:1 stoichiometry (N = 0.87 ± 0.05).

(F) Fluorescence-two-hybrid (F2H) analysis in live cells (Zolghadr et al., 2012) reveals that ALC1's ATPase (eYFP-ATPase; prey) readily enriches on a LacO-array tethered mCherry-LacI-macrodomain (bait). Example image (top images), quantitation (n = 20), and comparison with unrelated macrodomains reveal a specific ALC1 ATPase and ALC1 macrodomain interaction (bottom chart). Error bar represents the SEM, n ≥ 20.

See also Figures S1 and S2 and Table S1.

PARP1 Activation Disrupts the Auto-Inhibited State

ALC1 rapidly recruits to DNA damage sites and massively decompacts chromatin in response to PARP1 activation (Ahel et al., 2009; Gottschalk et al., 2009; Sellou et al., 2016). These activities require a functional, PAR-binding ALC1 macrodomain. We hypothesized that PAR binding to ALC1 may promote an active conformation of ALC1. To determine whether the activation of PARP1 in living cells alters the modular, intra-molecular interactions within ALC1, we used the F2H assay to measure the interaction of the ALC1 ATPase module with the macrodomain prior to and following UV-laser induced PARP1 activation. DNA damage leads to a time-dependent decrease of ALC1 ATPase prey from the tethered ALC1 macrodomain (Figure 2A; Movie S2). We conclude that PARP1 activation leads to the loss of interaction between the two ALC1 modules. H_2O_2-induced DNA damage also leads to a loss of interaction (Figure S2), and the site of PARP1 activation and ALC1 ATPase–macrodomain dissociation do not need to overlap, since FRAP assays indicate high turnover of our fusion proteins (Figure S2). Importantly, a G750E mutant within the macrodomain, which disrupts binding of the pyrophosphate of ADP-ribose in canonical macrodomains (Kustatscher et al., 2005), retains its binding with the ATPase module, even upon PARP1 induction (Figure S2). These data reveal that the interaction between the two ALC1 modules is regulated by PARP1 activation *in vivo*. PAR binding to the macrodomain is coupled to the loss of interaction with the ATPase module, consistent with a direct, allosteric regulation of ALC1 by PAR.

Next, we sought to determine the minimal ALC1 ligand that is necessary and sufficient to trigger ATPase–macrodomain dissociation and PAR-mediated ALC1 activation. We tested the effect of PARP1 activation *in vitro* on the interaction between ALC1 ATPase and macrodomain. Addition of NAD^+ to a pull-down containing PARP1, DNA, and the two ALC1 modules disrupts ALC1 ATPase–macrodomain interaction (Figure 2B, lanes 4 and 5). Addition of PARP1 inhibitors suppresses the disruptive effect of PARylation on ATPase–macrodomain interaction (lanes

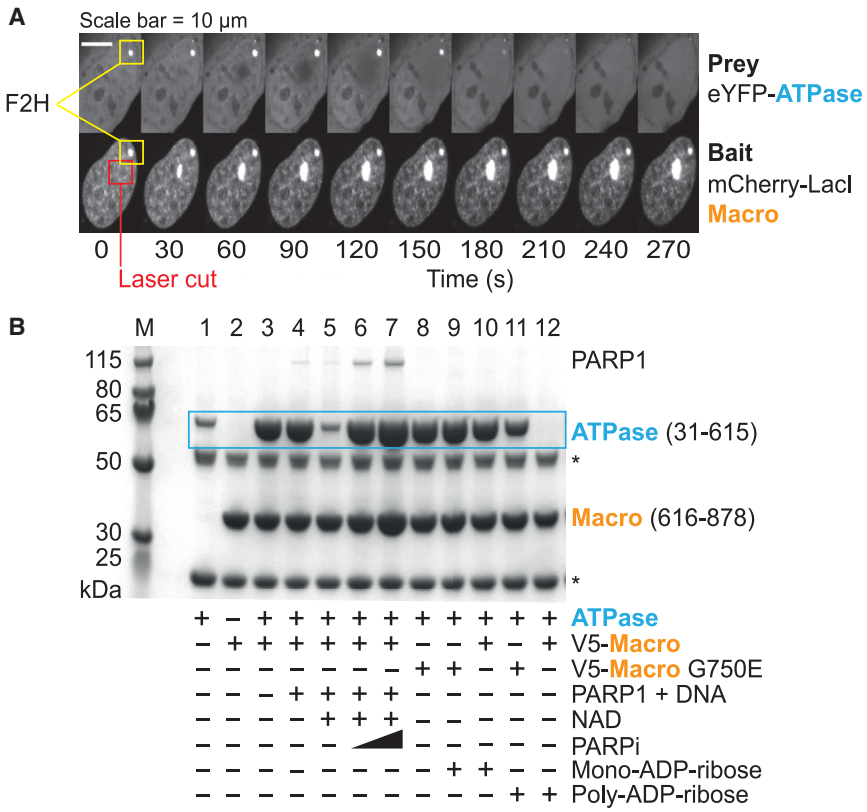

Figure 2. Acute DNA Damage and PARP1 Activation Trigger the Release of the ALC1 ATPase Module from a Tethered ALC1 Macrodomain

(A) The LacO-tethered LacI-ALC1 macrodomain module (bait) enriches ALC1's ATPase (prey) in the absence of exogenous DNA damage (left, compare white dot within the top and bottom yellow squares). Upon targeted and localized UV-laser-induced DNA damage (red square), the activation of the endogenous PARP1 enzyme leads to the dissociation of ALC1's ATPase module from the chromatin-tethered macrodomain (next panels). Upon DNA damage, the ALC1 macrodomain bait enriches at the DNA damage site, as expected from the local synthesis of its ligand poly-ADP-ribose, PAR (Ahel et al., 2009; Gottschalk et al., 2009). Both ALC1 recruitment (Ahel et al., 2009; Gottschalk et al., 2009) and the disruption of ATPase–macrodomain interactions require PARP1 activity.

(B) *In vitro* pull-down assays with V5-tagged ALC1 macrodomain reconstitute the PARP1 activity- and PAR-dependent dissociation of the modular ATPase–macrodomain interaction. Shown are lanes 1 and 2 with untagged ATPase and V5-tagged macro modules alone, respectively. Disruption of the ATPase–macrodomain complex requires PARP1, DNA and cofactor NAD^+ (lanes 3–5). Addition of small-molecule PARP1 inhibitors suppresses the PARP1 activity-dependent dissociation (lanes 6 and 7). The ALC1 ATPase–macrodomain complex is wholly disrupted by addition of pure PAR to the reaction, while a macrodomain point mutant (G750E), which alters ADP-ribose binding within its canonical ADP-ribose binding pocket, largely retains binding to the ALC1 ATPase module (lanes 11 and 12). In contrast to PAR, monomeric ADP-ribose fails to disrupt ATPase–macrodomain interactions for both wild-type and G750E mutant ALC1 macrodomain module (lanes 8–10). The asterisk denotes anti-V5 IgG heavy and light chains.

See also Figure S2.

6 and 7 versus lane 5). As expected, a point mutant within the ADP-ribose binding pocket of ALC1 (G750E) retains ATPase interaction (lane 8). Consistent with our *in vivo* observations (Figure S2), the interaction of the G750E macrodomain mutant with the ALC1 ATPase resists the addition of PAR (Figure 2B, lane 11). In sharp contrast, the wild-type macrodomain dissociates from the ATPase module upon PAR incubation (Figure 2B, lane 12). Thus, PAR *in vitro* is sufficient to dissociate the macrodomain of ALC1 from its ATPase. Further, dissociation requires a functional, PAR-binding macrodomain. Thus, PAR allosterically switches ALC1.

Synthetic Tri-ADP-Ribose Is a Nanomolar Effector of ALC1 Allostery

Macrodomains generally show high affinity for monomeric ADP-ribose (Karras et al., 2005; Kustatscher et al., 2005). Our ATPase–macrodomain competition assay, however, reveals that mono-ADP-ribose does not abrogate ALC1 ATPase–macrodomain interactions (Figure 2B, lane 10 versus lane 12), even when added in 100-fold molar excess, while PAR readily dissociates the complex. Consistently, ITC fails to detect an interaction between mono-ADP-ribose and the wild-type ALC1 macrodomain (Figure 3A; Table S2). Although key residues within the canonical ADP-ribose binding pocket of macrodomains are conserved in the PAR-binding ALC1 macrodomain, our data reveal that mono-ADP-ribose is not an ALC1 ligand.

We hypothesized that binding of PAR to ALC1 may require multiple ADP-ribose units. Interestingly, a PAR footprinting assay revealed that ALC1 protects oligomers of ~3 to >20 ADP-ribose units in length (Gottschalk et al., 2012). We therefore synthesized dimeric and trimeric forms of ADP-ribose (Kistemaker et al., 2015) and tested their binding to the ALC1 macrodomain. Remarkably, the ALC1 macrodomain binds di-ADP-ribose with a K_D = 3.7 μM and tri-ADP-ribose with nanomolar affinity (K_D = 10.6 nM; Figure 3A; Table S2). Extending ADP-ribose from monomer to trimer thus turns the NAD^+ metabolite into a high-affinity ligand. In sharp contrast to ALC1, the macrodomain of human histone macroH2A.1.1 recognizes mono-ADP-ribose and di-ADP-ribose with the same K_D (Figure S3). This indicates that ALC1 contains a NAD^+-metabolite binding surface that recognizes multiple features within tri-ADP-ribose. Highlighting the high affinity of the ALC1 macrodomain for tri-ADP-ribose, thermal shift assays reveal an ~10°C stabilization of the macrodomain by tri-ADP-ribose (Figure S3). To probe the selectivity of ALC1 toward related nucleotides, we conducted ITC with tri-adenylate RNA, tri-adenylate ssDNA, and penta-adenylate ssDNA. All fail to bind ALC1 (data not shown). Further, ITC and size-exclusion chromatography assays reveal a 1:1 complex

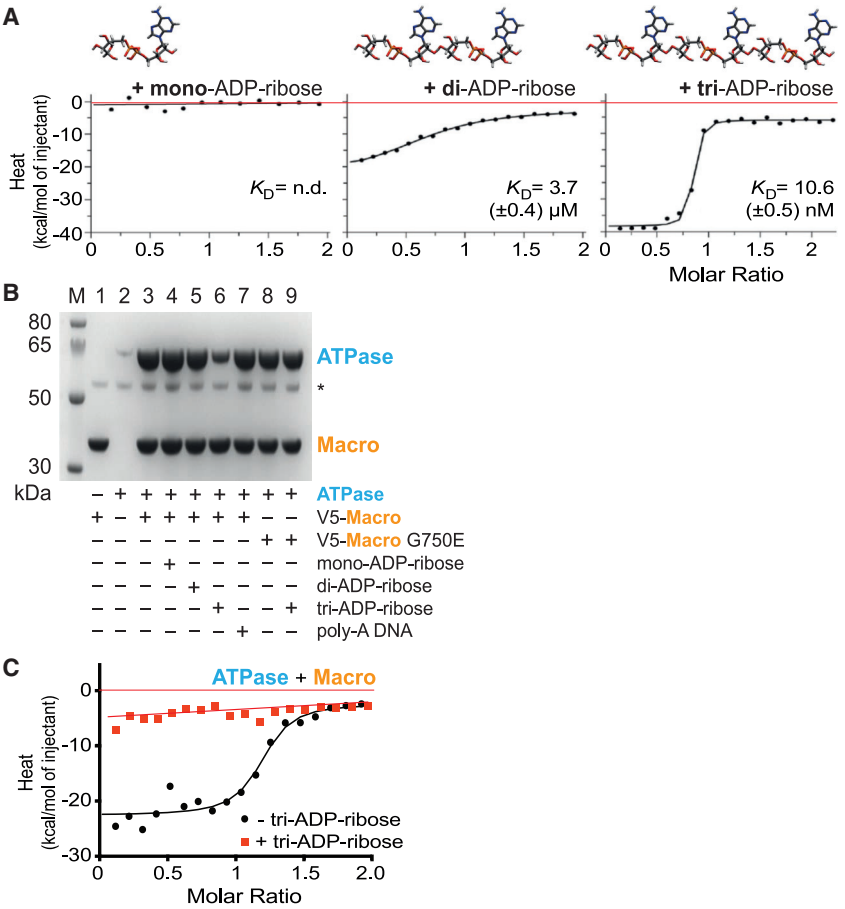

Figure 3. Tri-ADP-Ribose Is a Nanomolar Effector that Disrupts the Intramolecular ALC1 ATPase–Macrodomain Interaction

(A) ITC isotherms between the ALC1 macrodomain and mono-, di-, and tri-ADP-ribose. The Wiseman plot was not baseline subtracted to account for the heat of dilution of the ligands.

(B) SDS-PAGE of a V5-tagged ALC1 macrodomain pull-down with ALC1's ATPase. Addition of tri-ADP-ribose disrupts the interaction (lane 6 versus lane 3–5). In contrast, an ADP-ribose-binding pocket mutant (G750) suppresses the ability of tri-ADP-ribose to compete off the ALC1 ATPase module. Abrogation of the ATPase–macrodomain module interaction by tri-ADP-ribose thus requires an intact ADP-ribose binding pocket in the ALC1 macrodomain. The asterisk denotes anti-V5 IgG heavy chain.

(C) ITC isotherm for the interaction between the ALC1 macrodomain and ATPase in the presence (red squares) and absence (black circles) of tri-ADP-ribose. The Wiseman plot was not baseline subtracted.

See also Figure S3 and Table S2.

between the ALC1 macrodomain module and tri-ADP-ribose (Figures 3A and S3; Table S2). ALC1 seems unique among known macrodomain proteins in showing strong preference for oligo-ADP-ribose.

Our quantitative assays show that the ALC1 macrodomain reads oligomers of ADP-ribose. It can thus discriminate PAR and PARylation from other monomeric NAD+ metabolites and mono-ADP-ribosylated proteins. We hypothesize that the second and third ADP-ribose units of tri-ADP-ribose mediate additional contacts with ALC1 that extend beyond the protein's canonical ADP-ribose binding pocket, consistent with PAR footprinting data (Gottschalk et al., 2012).

Tri-ADP-Ribose Releases ALC1's Auto-Inhibition

The ability of tri-ADP-ribose to bind the ALC1 macrodomain with nanomolar affinity and high selectivity gives us a probe to dissect the allosteric activation of ALC1. We thus tested whether di- and tri-ADP-ribose mimic PAR at the functional level and disrupt ATPase–macrodomain interactions *in vitro*. V5-based pull-downs with tagged ALC1 macrodomain complexed to untagged ATPase show that the addition of di-ADP-ribose does not detectably affect interactions (Figure 3B; lane 5 versus lane 3). In contrast, addition of tri-ADP-ribose (in 2.5-fold molar excess) disrupts interactions between the two ALC1 modules (Figure 3B; lane 6 versus lane 3). Importantly, polyA-DNA does not cause macrodomain dissociation from the ALC1 ATPase, nor tri-ADP-ribose added to a PAR-binding deficient G750E macrodomain mutant (Figure 3B; lanes 7–9 versus lane 3). This indicates that trimeric ADP-ribose is sufficient to disrupt the intermolecular association between the two ALC1 modules. To quantitate the change in affinity between the two domains in the presence of the tri-ADP-ribose ligand, we conducted ITC assays of the ALC1 macrodomain with the ALC1 ATPase in the presence and absence of equimolar tri-ADP-ribose. Tri-ADP-ribose reduces the affinity between the two ALC1 modules from ~70 nM to below detection (K_D = > 50 μM; Figure 3C; Table S2). Tri-ADP-ribose thus reduces the affinity of the ALC1 macrodomain for the ATPase by at least three orders of magnitude. While we have been unable to obtain longer ADP-ribose oligomers, we conclude that the tri-ADP-ribose probe is an effective PAR mimic.

The NAD+ Metabolite Tri-ADP-Ribose Induces Conformational Changes within ALC1

Our assays indicate that tri-ADP-ribose may act as an allosteric trigger of the conformation and enzymatic activity of ALC1. To investigate how tri-ADP-ribose alters the structure of ALC1, we used H/D-exchange (HDX) measurements monitored by mass spectrometry (HDX-MS) to identify regions within ALC1 where the hydrogen bonding of the amide groups of the protein backbone change upon tri-ADP-ribose addition. Peptide segments resulting from pepsin proteolysis of ALC1, collectively covering 82.2% of the full-length sequence, were analyzed and used to resolve the HDX of ALC1 regions with and without tri-ADP-ribose (Figures 4A, S4, and S5). Upon binding tri-ADP-ribose, HDX-MS reveals increases in HDX corresponding to an increase in dynamics and destabilization of H-bonding. First, we observe

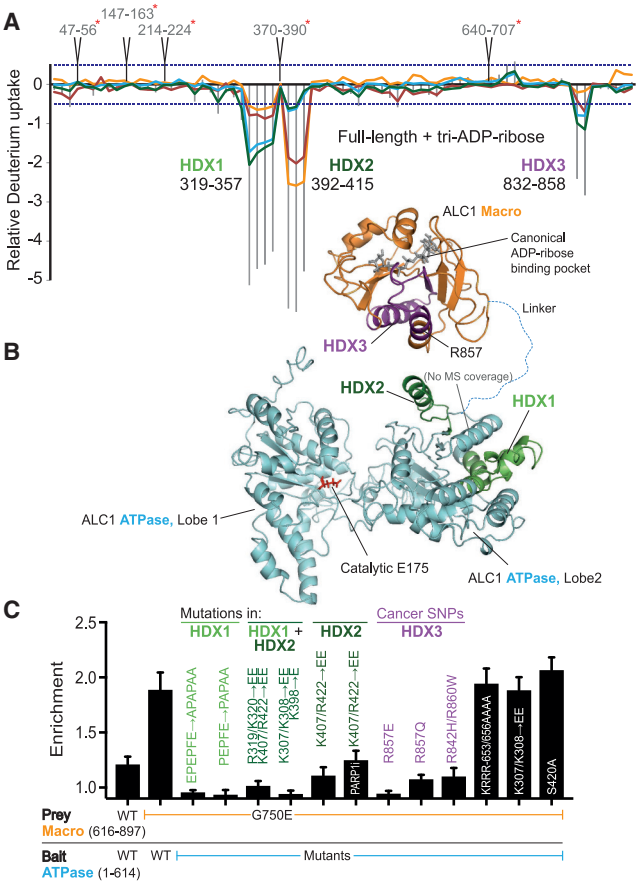

Figure 4. Ligand-Induced Ungating of the Auto-Inhibited ALC1 Remodeler

(A) HDX-MS analysis reveals concerted destabilization of H-bonding in ALC1 upon tri-ADP-ribose binding. Increased HDX is observed in peptides located in lobe 2 of the ALC1 ATPase (HDX1 and HDX2; residues shown) and surrounding the canonical ADP-ribose binding pocket of the ALC1 macrodomain (HDX3). Differences in HDX (ΔHDX, colored lines) between the unbound and ligand-bound state of ALC1 are plotted on the y axis with peptide number from N terminus to C terminus on the x axis. Negative values indicate increased HDX upon ligand binding. Values represent means of three independent measurements, and gray bars illustrate the sum of ΔHDX values for all sampled time points. Negative values indicate increased HDX upon ligand binding. Asterisks indicate ALC1 regions that were not resolved by MS (gray; see also Figure S4). Samples were incubated with D_2O for 0.25 min (orange), 1 min (red), 10 min (blue), and 60 min (green). The difference in HDX was considered significant if >0.5 (blue dashed line), corresponding to a 98.75% confidence interval; n = 3. (B) HDX results for ALC1 in the presence or absence of tri-ADP-ribose shown on I-TASSER (Roy et al., 2010) structural models of the ALC1 macrodomain and ATPase. Peptides that show a difference in HDX upon addition of tri-ADP ribose are colored purple in the macrodomain (top, HDX3) and green/lime in the ATPase (bottom, HDX1 and HDX2). The linker connecting the ATPase and macrodomain is shown as a dotted line (right). Its structure is not known, and it is largely not covered by our HDX data. Residues shown include R857 within the macrodomain's HDX3 region, a residue whose mutation is implicated in human gliomas, and the catalytic E175 in the ATPase as a reference for ALC1's active site. (C) Mutational analysis of HDX1, HDX2, and HDX3 using the F2H-based ATPase–macrodomain interaction assay. We targeted residues within HDX regions that contained patches of negative or positively charges, including the somatic cancer SNPs (R85Q, R842H, and R860W). Error bar represents the SEM, n ≥ 20. See also Figures S4 and S5.

changes within two neighboring segments encompassing a predicted α-helix in the ALC1 macrodomain, which lies in immediate proximity to the canonical mono-ADP-ribose ligand binding site (residues 832–858; HDX3; Figure 4B). This is consistent with the binding of tri-ADP-ribose within and near the canonical macrodomain pocket, leading to an altered H-bonding environment for residues involved in either (tri-) ADP-ribose interaction and/or intramolecular ALC1 contacts. Remarkably, tri-ADP-ribose binding to the ALC1 macrodomain also changes the HDX pattern of residues which are located in lobe 2 of the Snf2 ATPase, specifically residues 319–357 (HDX1) and 392–415 (HDX2; Figures 4A and 4B), which show distinct HDX increase. This indicates that the binding of tri-ADP-ribose to the macrodomain module of the ALC1 remodeler is associated with concerted changes in the H-bonding of regions in lobe 2 of the ATPase (Figure 4B).

Interestingly, in yChd1 and ISWI, the surface of the ATPase lobe 2 contacts the protein's chromodomain 1 and NTR region, respectively. This allows the remodelers to gate access of DNA to the ATPase motor. Our HDX-MS data reveal a destabilization of H-bonding and increased dynamics of lobe 2 within the ALC1 ATPase motor upon the binding of tri-ADP-ribose. Moreover, we observe tri-ADP-ribose-induced changes also near the canonical ADP-ribose binding pocket of the ALC1 macrodomain. HDX-MS data thus identify regions of ALC1 that undergo H-bond destabilization and conformational gating upon the allosteric activation induced by tri-ADP-ribose. We hypothesize that PAR binding to ALC1 may grant access of the ATPase motor to nucleosomal DNA, switching ALC1 into an "ungated" conformation that hydrolyzes ATP and slides nucleosomes.

Somatic Cancer Mutants Drive the Ungating of ALC1

To test whether the surface regions identified in our HDX-MS assays are important for the intramolecular interactions and enzymatic regulation of ALC1, we engineered point mutants in HDX1, HDX2, and HDX3 and tested how they affect ATPase–macrodomain interaction using F2H assays (Figure 4C). To increase the dynamic range of our assay, we used the ALC1 macrodomain G750E mutant, which binds PAR with lower affinity, as a reference. Interestingly, residues R857, R842, and R860 are mutated in human gliomas (Bamford et al., 2004). We find that the cancer SNPs R857Q and R842H/R860W, when introduced into the ALC1 macrodomain, reduce interaction with the ALC1 ATPase (Figure 4C). Similarly, point mutants within HDX1 and HDX2 of the ATPase module reduce ALC1 ATPase–macrodomain interactions (Figure 4C). We conclude that ALC1 regions identified in our HDX-MS analysis contribute to intramolecular ATPase–macrodomain interactions. Binding of tri-ADP-ribose to ALC1 disrupts intramolecular contacts that are critical for ALC1's auto-inhibition.

A Tethered ALC1 Fragment Remodels Chromatin *In Vivo*

The ability of PAR to activate ALC1 by releasing the interaction of ALC1's ATPase from the macrodomain predicts that ALC1 ATPase fragments lacking the PAR-regulated macrodomain might display chromatin remodeling activity *in vivo*, and without requiring PARP1 activation. Since PARP1 activation *in vivo* leads massively relaxes chromatin upon DNA damage and ALC1

mediates this chromatin plasticity (Sellou et al., 2016), we decided to use an *in vivo* chromatin relaxation assay to test the function of engineered ALC1 macrodomain-deletion fragments.

Since ALC1 does not recruit to chromatin upon DNA damage in the absence of its PAR-binding macrodomain, we tethered full-length, fragment, and mutant LacI-ALC1 fusions to an integrated LacO array in human cells. As expected, wild-type, full-length ALC1 (1–897) does not alter the LacO-array when tethered to the LacO-array (Figure 5A). In sharp contrast, when the macrodomain of ALC1 is deleted, the ALC1 fragment (residues 1–673) decompacts the LacO array (Figure 5A). This chromatin relaxation is seen with other ALC1 C-terminal fragments, but not in a fragment as short as 1–614. This indicates that sequences within linker II of ALC1 (residues 615–673; Figure 1A) promote chromatin remodeling activity, while the macrodomain is inhibitory to ALC1 *in vivo*. Importantly, mutation of conserved residues within the ALC1 helicase that disrupt ATPase activity (Ahel et al., 2009; Gottschalk et al., 2009) abolishes ALC1-induced chromatin relaxation (Figure 5A). Tethered ALC1 fragments lacking the macrodomain thus possess remodeling activity in the absence of DNA damage induction and PARP1 activation.

Next, we tested whether the macrodomain of ALC1 alters the inherent chromatin remodeling activity of the LacI-tethered ALC1 ATPase (1–673) construct when added in *trans*. Addition of the ALC1 macrodomain module to the active, tethered ALC1 ATPase reduces chromatin decompaction (Figure 5A). A PARP1 inhibitor enhances this inhibition. Our data indicate that the ALC1 macrodomain inhibits the ATPase activity of ALC1 at physiological levels of PARP1 activity. In its absence, a tethered ALC1 ATPase module remodels chromatin *in vivo.*

Tri-ADP-Ribose De-represses the ATPase Activity of the ALC1 Remodeler

Our LacO-tethering assay identified a constitutively active ALC1 ATPase fragment (1–673), whose activity can be suppressed by addition of the ALC1 macrodomain module. Since tri-ADP-ribose promotes the dissociation of the ALC1 macrodomain from the ALC1 ATPase module, we sought to determine the relevance of tri-ADP-ribose binding on the catalytic activity of the ALC1 remodeler. We established a robust, DNA-dependent ATPase assay for both the ALC1 ATPase module (31–673) and the (near) full-length ALC1 protein (31–878). We find that the ALC1 ATPase module shows robust, DNA-dependent ATPase activity (Figure S6). Importantly, titration of the ALC1 macrodomain module to the ALC1 ATPase lowers ATPase activity (Figure S6). Once a 2.5 molar excess of ALC1 macrodomain is added to the ALC1 ATPase, the resulting complex is inactive, revealing background ATPase activity similar to that of the ALC1 ATPase without DNA. The ALC1 macrodomain thus represses the inherent ATPase activity present in the ALC1 ATPase module.

Next, we tested whether the addition of the nanomolar tri-ADP-ribose ligand of ALC1 alters the ATPase activity of the enzyme *in vitro*. Addition of a 2-fold molar excess of tri-ADP-ribose to the inactive ALC1 ATPase–macrodomain complex robustly de-represses the ALC1 ATPase, going from <2% without tri-ADP-ribose to ~60% of the activity of the free ALC1 ATPase module (Figure 5B). Importantly, addition of a 6-fold molar excess of mono-ADP-ribose to the ATPase–macrodomain complex fails to rescue ATPase activity (Figure 5B), consistent with the lack of binding of monomeric ADP-ribose for the ALC1 macrodomain (Figure 3A). Thus, tri-ADP-ribose binding to the ALC1 ATPase–macrodomain complex strongly activates the ATPase activity of the ALC1 remodeler.

In addition, we tested whether tri-ADP-ribose alters the activity of (near) full-length ALC1. As expected, the ATPase activity of this construct is low, including in the presence of mono-ADP-ribose. However, tri-ADP-ribose strongly activates the ATPase activity in the ALC1 remodeler (Figure 5C). The level of activation (fold induction) induced by tri-ADP-ribose is lower than in our assays using the reconstituted ALC1 complex. However, this is likely the result of degradation products present in our recombinant ALC1 (31–878) construct (Figure S6). Indeed, some of the proteolytic fragments observed in our ALC1 construct (31–878) likely lack (parts of) the inhibitory macrodomain and may thus display catalytic ATPase activity independently of the tri-ADP-ribose trigger. Our assays show that tri-ADP-ribose is a potent activator of the DNA-dependent ATPase activity of the ALC1 remodeler.

Somatic Cancer Mutants in ALC1 Drive Chromatin Remodeling

We identified cancer SNPs located within the HDX3 region of the ALC1 macrodomain, which lead to a loss-of-interaction phenotype between the ALC1 ATPase and macrodomain (Figure 4C). We thus tested the effect of these mutant macrodomains on the activity of the constitutively active ALC1 ATPase tethered to the LacO array when expressed in *trans*. Interestingly, the point mutants R857Q and R842H/R860W show a decompaction of the LacO similar to that of the constitutively active ALC1 ATPase module without any macrodomain expressed in *trans*. In sharp contrast, co-expression of the wild-type macrodomain, or of the G750E macrodomain mutant, strongly reduces the decompacted area, indicating that these macrodomain constructs inhibit the remodeler activity in *trans* and *in vivo* (Figure 5A). Furthermore, FCS assays in the context of the full-length ALC1 protein show a decreased diffusion behavior of the HDX1 and HDX3 mutants compared to wild-type ALC1 (Figure S6). This suggests that HDX mutants that disrupt the intramolecular ATPase–macrodomain interactions promote an ungated structure in ALC1, which may potentially lead to increased DNA binding. Taken together, our data show that somatic cancer mutations phenocopy the activity of the constitutively active ALC1 ATPase fragment. While the relevance for this in cancer remains to be established, our tethering assay indicates that mutations in ALC1 that disrupt its inhibitory intra-molecular interactions (Figure 4C) promote the deregulated, constitutive activity of this chromatin remodeler (Figure 5A).

Modular Allostery in ALC1 Regulates Interaction with PARP1

To further probe the PAR-regulated modular allostery in ALC1, we tested whether, in turn, the ATPase module affects the ability of the ALC1 macrodomain to recognize its effector molecule, PARylated PARP1, in living cells. While full-length ALC1 does not readily interact with full-length PARP1 in untreated human cells using the F2H assay (Figure 5D; Movie S3), DNA damage induction with H_2O_2 promotes the interaction between

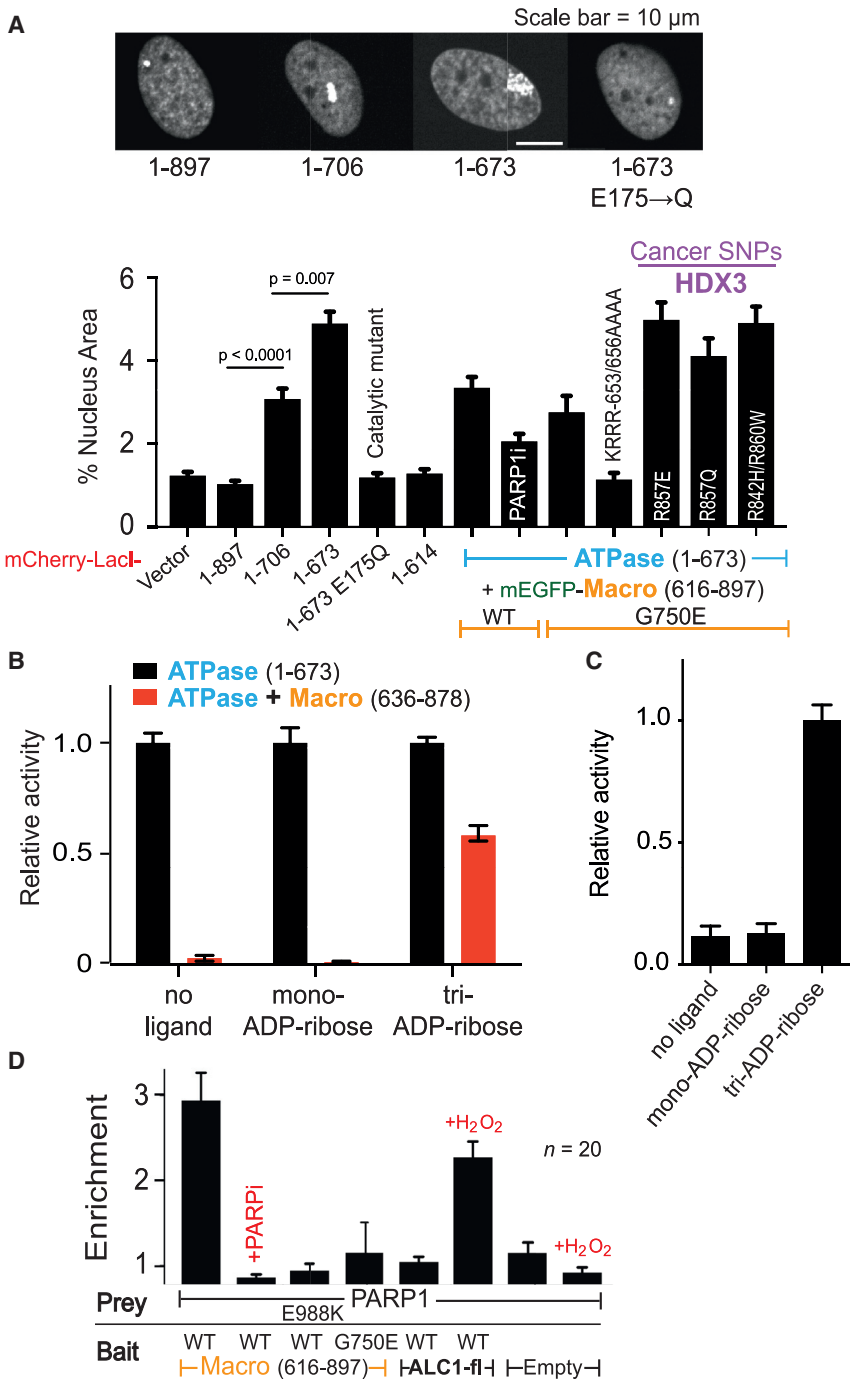

Figure 5. Release from Auto-Inhibition Drives ALC1's Chromatin Remodeling Activity

(A) Tethering of engineered mCherry-LacI-ALC1 to an integrated LacO array decompacts chromatin in U2OS cells (representative images; top). The decompaction of the LacO array is calculated as percent of the nucleus area (bottom). The deletion of ALC1's macrodomain generates a constitutively active ALC1 that decompacts the LacO-array *in vivo*. Constructs assayed: full-length ALC1 (1–897), macrodomain deletion (1–707), a hyperactive construct (1–673), ATPase-dead point mutation (1–673, E175Q), plus ALC1 (1–614), which represents the ATPase module identified in our limited proteolysis (Figure S1). Importantly, co-transfection of the ALC1 macrodomain (mEGFP-616–897) with the constitutively active ALC1 fragment (1–673) reduces the decompacted area. Further, cancer SNPs within HDX3 that disrupt interaction with the ATPase module (Figure 4C) do not decrease the chromatin decompaction catalyzed by the ALC1 ATPase (1–673) module. Error bar represents the SEM, n ≥ 20.

(B) Tri-ADP-ribose de-represses the ATPase activity of the inactive ALC1 ATPase–macrodomain complex. The DNA-dependent ATPase activity of the ALC1 ATPase module was measured using a malachite green assay in the presence and absence of a 2.5 molar excess of ALC1 macrodomain module, as well as in the absence (left) or presence of either a 6-fold molar excess of ADP-ribose (middle) or a 2-fold molar excess of tri-ADP-ribose (right). The data are normalized to the respective mean activity of the ATPase module alone (black bars; n = 3; mean ± SEM).

(C) Tri-ADP-ribose promotes the activation of the ALC1 chromatin remodeling enzyme. The (near) full-length ALC1 construct (31–878) shows only basal ATPase activity in the absence or presence of a 15-fold molar excess of ADP-ribose. In contrast, a 5-fold molar excess of tri-ADP-ribose greatly stimulates ALC1-catalyzed and dsDNA-dependent ATP hydrolysis. The data are normalized to the mean value of ALC1 activity in the presence of tri-ADP-ribose (n = 3; mean ± SEM).

(D) F2H assay testing the interaction of tethered ALC1 macrodomain (wild-type, WT; G750E mutant) with fluorescently tagged PARP1 (wild-type and E988K PAR elongation mutant). Indicated experiments were done in the presence of a PARP1 inhibitor (+PARPi) or H_2O_2. Error bar represents the SEM, n ≥ 20.

See also Figure S6.

these two proteins, consistent with the recognition of activated, PARylated PARP1 by ALC1. Interestingly, an ALC1 fragment lacking the catalytic ATPase domain readily interacts with PARP1, even in the absence of exogenous DNA damage (Figure 5D). Treatment of cells with a PARP1 inhibitor abrogates this interaction. This indicates that the isolated macrodomain of ALC1 recognizes ADP-ribosylated forms of PARP1 under "non-DNA-damage" conditions (Figure 5D), likely reflecting background ADP-ribosylation. Consistently, a point mutant in the ALC1 macrodomain that reduces PAR binding (G750E), or mutation of a key residue in PARP1 (E988K) that is responsible for the elongation of mono-ADP-ribosyl-PARP1 to poly-ADP-ribosyl-PARP1, disrupts the interaction between the ALC1 macrodomain and PARP1 (Figure 5D). We conclude that the isolated ALC1 macrodomain interacts with ADP-ribosylated PARP1 under physiological conditions, while full-length ALC1 requires a

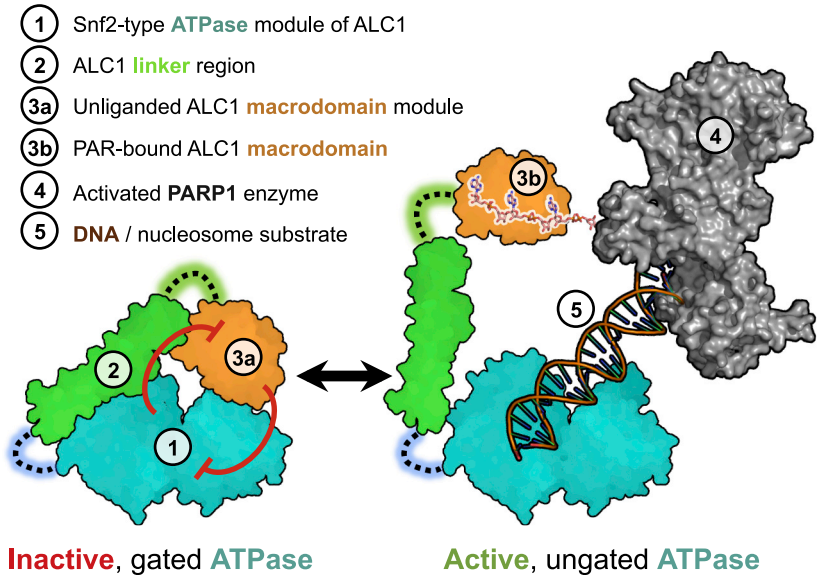

Figure 6. Modular Allostery Sets a Threshold for PARP1-Induced ALC1 Activation

Modular allostery in the chromatin remodeler ALC1 regulates auto-inhibition through the reciprocal interaction of ALC1's ATPase and macrodomain modules. This helps to ensure that the PARP1 product PAR acts as an allosteric activator and potent trigger of ALC1-promoted chromatin relaxation only once acute DNA damage has induced PARP1 activity.

high threshold of DNA damage and PARP1 activation in order to interact with PARylated PARP1. Thus, the ATPase of ALC1 lowers the affinity of the macrodomain for PARylated-PARP1, consistent with modular allostery. We suggest that the modularity of ALC1 allows the remodeler to be activated only once a threshold of PARP1 activation has been reached.

DISCUSSION

Auto-inhibitory interactions play important roles in signaling and in the regulation of chromatin and repair factors (DaRosa et al., 2015; Guo et al., 2015). Considering the emergent role of remodelers in cancer (St Pierre and Kadoch, 2017; Zhao et al., 2017), a better understanding of how DNA damage alters chromatin is important. While the mechanisms that ALC1 and CHD2 employ to relax chromatin upon DNA damage *in vivo* (Movie S1) are not known, and the remodelers' substrate(s) *in vivo* remains to be identified, here we have identified and dissected the mechanisms that allow the oncogene ALC1 to be tightly regulated by the NAD^+ metabolite PAR (Figure 6). We show that reciprocal interactions between the ALC1 ATPase and its macrodomain allow ALC1 activity to be controlled by PARP1 activation. The binding of an oligomer of at least three ADP-ribose units to ALC1's macrodomain triggers conformational changes that disrupt auto-inhibitory interactions. This "ungates" the ATPase module, promoting DNA-dependent ATPase activity *in vitro* and remodeling *in vivo* (Figures 3, 4, and 5). Modular allostery thus ensures that ALC1 is exquisitely sensitive to and selective for oligomeric forms of ADP-ribose. We infer that PAR acts as a catalytic trigger only once a threshold of PARP1 induction has been reached. Most "reader" modules in chromatin biology are thought to play a recruitment and tethering function. Our identification of a reciprocal interaction between a PAR-binding macrodomain ("reader" module) and the catalytic ATPase module of ALC1 adds to the allostery described for DNA methyltransferases (Guo et al., 2015; Jeltsch and Jurkowska, 2016).

In vivo, binding of the PAR effector to the macrodomain occurs when ALC1 recruits to DNA damage sites, which tethers the remodeler to chromatin and allows ALC1 to remodel chromatin. Our study does not identify the specific, physiological substrate that ALC1 remodels on chromatin. Swi2/Snf2 remodelers such as Mot1 remodel non-nucleosomal substrates (Wollmann et al., 2011). *In vivo*, the PARylation of histones, PARP1, ALC1, and/or other chromatin factors may thus contribute to how ALC1 catalyzes chromatin relaxation.

The selectivity of ALC1 toward oligo-ADP-ribose, and the fact that the enzyme's ATPase impairs the ability of ALC1's macrodomain to bind PARP1 under non-DNA damage conditions (Figure 5D), likely helps to ensure that PARP1-dependent chromatin relaxation is only catalyzed once PARP1 has been activated, such as during DNA damage. Our data reveal how the ATPase activity of a remodeler is gated by the PARP1-product and nucleic acid PAR through regulatory interactions mediated by ALC1's macrodomain. This adds to our mechanistic understanding of how the ATPase activity of chromatin remodelers is regulated. Further work will be necessary to dissect how poly-ADP-ribosylated PARP1 promotes the efficient remodeling of nucleosomes. Our data show that in the special case of ALC1, tethering and activation occur through a NAD^+ metabolite, which acts as an allosteric ATPase trigger, in a mechanism mediated by the remodeler's core macrodomain fold and additional contacts with the PAR ligand.

Our analysis also identifies how the oncogene ALC1 might be targeted in cancer. Small molecules that inhibit its allostery or activity should reproduce *ALC1* knockdown phenotypes, such as reduced tumor growth, reduced reprogramming, and increased sensitivity to chemotherapy (Jiang et al., 2015; Liu et al., 2016). Compounds that stabilize the inactive, gated conformation of ALC1, which lower its catalytic activity, or that disrupt its ability to recognize PAR should suppress the potent chromatin relaxation activity of this oncogene.

STAR★METHODS

Detailed methods are provided in the online version of this paper and include the following:

- KEY RESOURCES TABLE
- CONTACT FOR REAGENT AND RESOURCE SHARING

- METHOD DETAILS
  - Cloning, protein expression and purification
  - Limited trypsin proteolysis
  - Full-length ALC1 baculovirus cloning expression and purification
  - Hydrogen deuterium exchange mass-spectrometry (HDX-MS)
  - Chemical cross-linking coupled to mass spectrometry (XL-MS)
  - Isothermal titration calorimetry (ITC) assays
  - Plasmids for cellular assays
  - Cell culture and transfections
  - Microscopy experiments
  - UV-laser micro-irradiation assays
  - PARP1 inhibitor treatment and H_2O_2 treatments
  - Fluorescence two-hybrid (F2H) assay
  - Co-immunoprecipitation assays
  - LacO array remodelling assays
  - V5-Macrodomain pull-down assays
  - Fluorescence correlation spectroscopy (FCS)
  - Thermal shift assays
  - Chromatin remodeler ATPase assays
  - Analytical size exclusion chromatography (aSEC)
- QUANTIFICATION AND STATISTICAL ANALYSIS
  - For *in vitro* ATPase and Thermofluor assays
  - For the F2H and lacO array assays
  - For HDX-MS measurements

SUPPLEMENTAL INFORMATION

Supplemental Information includes six figures, three tables, and three movies and can be found with this article at https://doi.org/10.1016/j.molcel.2017.11.019.

ACKNOWLEDGMENTS

We thank Julia Preisser and Zeinab Paya for technical help. We thank Evi Soutoglou for U2OS cells harboring a stably integrated LacO array, and the Biophysics Facility of the Biomedical Center Munich and the Microscopy Rennes Imaging Center (BIOSIT, Université Rennes 1) for technical assistance. We thank the Ignasi Forné and Axel Imhof for mass spectrometry analyses. We thank Alexander Brehm, Michael Hothorn, and members of our labs for comments. We thank Karl-Peter Hopfner for assisting this project and for financially supporting S.E. This project was made possible by funding from the Netherlands Organization for Scientific Research (to H.A.V.K.), the Danish Council for Independent Research (0602-02740B to K.D.R.), and the DFG (LA 2489/1-1 and SFB1064 to A.G.L.; MU 3613/1-1 and SFB1064 to F.M.P.).

AUTHOR CONTRIBUTIONS

Conceptualization, H.R.S., M.H., G.T., and A.G.L.; Methodology, H.R.S., A.P.N., I.R.M., G.K., F.M.P., G.T., K.D.R., and A.G.L.; Investigation, H.R.S., A.P.N., I.R.M., G.K., M.H., N.H., C.B., C.K., and S.H.; Formal Analysis, H.R.S., A.P.N., I.R.M., G.K., M.H., N.H., C.B., F.M.P., G.T., K.D.R., and A.G.L.; Writing – Original Draft, H.R.S. and A.G.L.; Writing – Review & Editing, H.R.S., G.K., and A.G.L.; Funding Acquisition, H.A.V.K., D.V.F., F.M.P., and A.G.L.; Resources, H.A.V.K., D.V.F., S.E., S.H., and C.K.; Supervision, S.H., F.M.P., G.T., K.D.R., and A.G.L.

Received: June 28, 2017
Revised: October 5, 2017
Accepted: November 15, 2017
Published: December 7, 2017

REFERENCES

Ahel, D., Horejsí, Z., Wiechens, N., Polo, S.E., Garcia-Wilson, E., Ahel, I., Flynn, H., Skehel, M., West, S.C., Jackson, S.P., et al. (2009). Poly(ADP-ribose)-dependent regulation of DNA repair by the chromatin remodeling enzyme ALC1. Science *325*, 1240–1243.

Altmeyer, M., Neelsen, K.J., Teloni, F., Pozdnyakova, I., Pellegrino, S., Grøfte, M., Rask, M.-B.D., Streicher, W., Jungmichel, S., Nielsen, M.L., and Lukas, J. (2015). Liquid demixing of intrinsically disordered proteins is seeded by poly(ADP-ribose). Nat. Commun. *6*, 8088.

Asher, G., Reinke, H., Altmeyer, M., Gutierrez-Arcelus, M., Hottiger, M.O., and Schibler, U. (2010). Poly(ADP-ribose) polymerase 1 participates in the phase entrainment of circadian clocks to feeding. Cell *142*, 943–953.

Bai, P., Canto, C., Brunyánszki, A., Huber, A., Szántó, M., Cen, Y., Yamamoto, H., Houten, S.M., Kiss, B., Oudart, H., et al. (2011a). PARP-2 regulates SIRT1 expression and whole-body energy expenditure. Cell Metab. *13*, 450–460.

Bai, P., Cantó, C., Oudart, H., Brunyánszki, A., Cen, Y., Thomas, C., Yamamoto, H., Huber, A., Kiss, B., Houtkooper, R.H., et al. (2011b). PARP-1 inhibition increases mitochondrial metabolism through SIRT1 activation. Cell Metab. *13*, 461–468.

Bamford, S., Dawson, E., Forbes, S., Clements, J., Pettett, R., Dogan, A., Flanagan, A., Teague, J., Futreal, P.A., Stratton, M.R., and Wooster, R. (2004). The COSMIC (Catalogue of Somatic Mutations in Cancer) database and website. Br. J. Cancer *91*, 355–358.

Bowman, A., Lercher, L., Singh, H.R., Zinne, D., Timinszky, G., Carlomagno, T., and Ladurner, A.G. (2016). The histone chaperone sNASP binds a conserved peptide motif within the globular core of histone H3 through its TPR repeats. Nucleic Acids Res. *44*, 3105–3117.

Cambronne, X.A., Stewart, M.L., Kim, D., Jones-Brunette, A.M., Morgan, R.K., Farrens, D.L., Cohen, M.S., and Goodman, R.H. (2016). Biosensor reveals multiple sources for mitochondrial NAD^+. Science *352*, 1474–1477.

Carter-O'Connell, I., Jin, H., Morgan, R.K., Zaja, R., David, L.L., Ahel, I., and Cohen, M.S. (2016). Identifying family-member-specific targets of mono-ARTDs by using a chemical genetics approach. Cell Rep. *14*, 621–631.

Chen, L., Chan, T.H.M., Yuan, Y.-F., Hu, L., Huang, J., Ma, S., Wang, J., Dong, S.-S., Tang, K.H., Xie, D., et al. (2010). CHD1L promotes hepatocellular carcinoma progression and metastasis in mice and is associated with these processes in human patients. J. Clin. Invest. *120*, 1178–1191.

Chou, D.M., Adamson, B., Dephoure, N.E., Tan, X., Nottke, A.C., Hurov, K.E., Gygi, S.P., Colaiácovo, M.P., and Elledge, S.J. (2010). A chromatin localization screen reveals poly (ADP ribose)-regulated recruitment of the repressive polycomb and NuRD complexes to sites of DNA damage. Proc. Natl. Acad. Sci. USA *107*, 18475–18480.

Clapier, C.R., and Cairns, B.R. (2012). Regulation of ISWI involves inhibitory modules antagonized by nucleosomal epitopes. Nature *492*, 280–284.

Czarna, A., Berndt, A., Singh, H.R., Grudziecki, A., Ladurner, A.G., Timinszky, G., Kramer, A., and Wolf, E. (2013). Structures of *Drosophila* cryptochrome and mouse cryptochrome1 provide insight into circadian function. Cell *153*, 1394–1405.

Dann, G.P., Liszczak, G.P., Bagert, J.D., Müller, M.M., Nguyen, U.T.T., Wojcik, F., Brown, Z.Z., Bos, J., Panchenko, T., Pihl, R., et al. (2017). ISWI chromatin remodellers sense nucleosome modifications to determine substrate preference. Nature *548*, 607–611.

DaRosa, P.A., Wang, Z., Jiang, X., Pruneda, J.N., Cong, F., Klevit, R.E., and Xu, W. (2015). Allosteric activation of the RNF146 ubiquitin ligase by a poly(ADP-ribosyl)ation signal. Nature *517*, 223–226.

Fitzgerald, D.J., Berger, P., Schaffitzel, C., Yamada, K., Richmond, T.J., and Berger, I. (2006). Protein complex expression by using multigene baculoviral vectors. Nat. Methods *3*, 1021–1032.

Gibson, B.A., Zhang, Y., Jiang, H., Hussey, K.M., Shrimp, J.H., Lin, H., Schwede, F., Yu, Y., and Kraus, W.L. (2016). Chemical genetic discovery of PARP targets reveals a role for PARP-1 in transcription elongation. Science *353*, 45–50.

Gottschalk, A.J., Timinszky, G., Kong, S.E., Jin, J., Cai, Y., Swanson, S.K., Washburn, M.P., Florens, L., Ladurner, A.G., Conaway, J.W., and Conaway, R.C. (2009). Poly(ADP-ribosyl)ation directs recruitment and activation of an ATP-dependent chromatin remodeler. Proc. Natl. Acad. Sci. USA *106*, 13770–13774.

Gottschalk, A.J., Trivedi, R.D., Conaway, J.W., and Conaway, R.C. (2012). Activation of the SNF2 family ATPase ALC1 by poly(ADP-ribose) in a stable ALC1·PARP1·nucleosome intermediate. J. Biol. Chem. *287*, 43527–43532.

Grundy, G.J., Polo, L.M., Zeng, Z., Rulten, S.L., Hoch, N.C., Paomephan, P., Xu, Y., Sweet, S.M., Thorne, A.W., Oliver, A.W., et al. (2016). PARP3 is a sensor of nicked nucleosomes and monoribosylates histone H2BGlu2. Nat. Commun. *7*, 1–12.

Guo, X., Wang, L., Li, J., Ding, Z., Xiao, J., Yin, X., He, S., Shi, P., Dong, L., Li, G., et al. (2015). Structural insight into autoinhibition and histone H3-induced activation of DNMT3A. Nature *517*, 640–644.

Hauk, G., McKnight, J.N., Nodelman, I.M., and Bowman, G.D. (2010). The chromodomains of the Chd1 chromatin remodeler regulate DNA access to the ATPase motor. Mol. Cell *39*, 711–723.

Jankevicius, G., Hassler, M., Golia, B., Rybin, V., Zacharias, M., Timinszky, G., and Ladurner, A.G. (2013). A family of macrodomain proteins reverses cellular mono-ADP-ribosylation. Nat. Struct. Mol. Biol. *20*, 508–514.

Jeltsch, A., and Jurkowska, R.Z. (2016). Allosteric control of mammalian DNA methyltransferases - a new regulatory paradigm. Nucleic Acids Res. *44*, 8556–8575.

Jiang, B.-H., Chen, W.-Y., Li, H.-Y., Chien, Y., Chang, W.-C., Hsieh, P.-C., Wu, P., Chen, C.-Y., Song, H.-Y., Chien, C.-S., et al. (2015). CHD1L regulated PARP1-driven pluripotency and chromatin remodeling during the early-stage cell reprogramming. Stem Cells *33*, 2961–2972.

Karras, G.I., Kustatscher, G., Buhecha, H.R., Allen, M.D., Pugieux, C., Sait, F., Bycroft, M., and Ladurner, A.G. (2005). The macro domain is an ADP-ribose binding module. EMBO J. *24*, 1911–1920.

Kim, M.Y., Mauro, S., Gévry, N., Lis, J.T., and Kraus, W.L. (2004). NAD^+-dependent modulation of chromatin structure and transcription by nucleosome binding properties of PARP-1. Cell *119*, 803–814.

Kistemaker, H.A.V., Lameijer, L.N., Meeuwenoord, N.J., Overkleeft, H.S., van der Marel, G.A., and Filippov, D.V. (2015). Synthesis of well-defined adenosine diphosphate ribose oligomers. Angew. Chem. Int. Ed. Engl. *54*, 4915–4918.

Kruhlak, M.J., Celeste, A., Dellaire, G., Fernandez-Capetillo, O., Müller, W.G., McNally, J.G., Bazett-Jones, D.P., and Nussenzweig, A. (2006). Changes in chromatin structure and mobility in living cells at sites of DNA double-strand breaks. J. Cell Biol. *172*, 823–834.

Kulkarni, A., Oza, J., Yao, M., Sohail, H., Ginjala, V., Tomás-Loba, A., Horejsi, Z., Tan, A.R., Boulton, S.J., and Ganesan, S. (2013). Tripartite Motif-containing 33 (TRIM33) protein functions in the poly(ADP-ribose) polymerase (PARP)-dependent DNA damage response through interaction with Amplified in Liver Cancer 1 (ALC1) protein. J. Biol. Chem. *288*, 32357–32369.

Kustatscher, G., Hothorn, M., Pugieux, C., Scheffzek, K., and Ladurner, A.G. (2005). Splicing regulates NAD metabolite binding to histone macroH2A. Nat. Struct. Mol. Biol. *12*, 624–625.

Liu, M., Chen, L., Ma, N.-F., Chow, R.K.K., Li, Y., Song, Y., Chan, T.H.M., Fang, S., Yang, X., Xi, S., et al. (2016). CHD1L promotes lineage reversion of hepatocellular carcinoma through opening chromatin for key developmental transcription factors. Hepatology *63*, 1544–1559.

Lord, C.J., and Ashworth, A. (2017). PARP inhibitors: Synthetic lethality in the clinic. Science *355*, 1152–1158.

Ludwigsen, J., Pfennig, S., Singh, A.K., Schindler, C., Harrer, N., Forné, I., Zacharias, M., and Mueller-Planitz, F. (2017). Concerted regulation of ISWI by an autoinhibitory domain and the H4 N-terminal tail. eLife *6*, e21477.

Luijsterburg, M.S., de Krijger, I., Wiegant, W.W., Shah, R.G., Smeenk, G., de Groot, A.J.L., Pines, A., Vertegaal, A.C.O., Jacobs, J.J.L., Shah, G.M., and van Attikum, H. (2016). PARP1 links CHD2-mediated chromatin expansion and H3.3 deposition to DNA repair by non-homologous end-joining. Mol. Cell *61*, 547–562.

Ma, N.-F., Hu, L., Fung, J.M., Xie, D., Zheng, B.-J., Chen, L., Tang, D.-J., Fu, L., Wu, Z., Chen, M., et al. (2008). Isolation and characterization of a novel oncogene, amplified in liver cancer 1, within a commonly amplified region at 1q21 in hepatocellular carcinoma. Hepatology *47*, 503–510.

Mueller-Planitz, F. (2015). Crossfinder-assisted mapping of protein crosslinks formed by site-specifically incorporated crosslinkers. Bioinformatics *31*, 2043–2045.

Murawska, M., Hassler, M., Renkawitz-Pohl, R., Ladurner, A., and Brehm, A. (2011). Stress-induced PARP activation mediates recruitment of *Drosophila* Mi-2 to promote heat shock gene expression. PLoS Genet. *7*, e1002206.

Petesch, S.J., and Lis, J.T. (2012). Activator-induced spread of poly(ADP-ribose) polymerase promotes nucleosome loss at Hsp70. Mol. Cell *45*, 64–74.

Poirier, G.G., de Murcia, G., Jongstra-Bilen, J., Niedergang, C., and Mandel, P. (1982). Poly(ADP-ribosyl)ation of polynucleosomes causes relaxation of chromatin structure. Proc. Natl. Acad. Sci. USA *79*, 3423–3427.

Polo, S.E., Kaidi, A., Baskcomb, L., Galanty, Y., and Jackson, S.P. (2010). Regulation of DNA-damage responses and cell-cycle progression by the chromatin remodelling factor CHD4. EMBO J. *29*, 3130–3139.

Rosenthal, F., Feijs, K.L.H., Frugier, E., Bonalli, M., Forst, A.H., Imhof, R., Winkler, H.C., Fischer, D., Caflisch, A., Hassa, P.O., et al. (2013). Macrodomain-containing proteins are new mono-ADP-ribosylhydrolases. Nat. Struct. Mol. Biol. *20*, 502–507.

Roy, A., Kucukural, A., and Zhang, Y. (2010). I-TASSER: a unified platform for automated protein structure and function prediction. Nat. Protoc. *5*, 725–738.

Schindelin, J., Arganda-Carreras, I., Frise, E., Kaynig, V., Longair, M., Pietzsch, T., Preibisch, S., Rueden, C., Saalfeld, S., Schmid, B., et al. (2012). Fiji: an open-source platform for biological-image analysis. Nat. Methods *9*, 676–682.

Sellou, H., Lebeaupin, T., Chapuis, C., Smith, R., Hegele, A., Singh, H.R., Kozlowski, M., Bultmann, S., Ladurner, A.G., Timinszky, G., and Huet, S. (2016). The poly(ADP-ribose)-dependent chromatin remodeler Alc1 induces local chromatin relaxation upon DNA damage. Mol. Biol. Cell *27*, 3791–3799.

Sharifi, R., Morra, R., Appel, C.D., Tallis, M., Chioza, B., Jankevicius, G., Simpson, M.A., Matic, I., Ozkan, E., Golia, B., et al. (2013). Deficiency of terminal ADP-ribose protein glycohydrolase TARG1/C6orf130 in neurodegenerative disease. EMBO J. *32*, 1225–1237.

Smeenk, G., Wiegant, W.W., Marteijn, J.A., Luijsterburg, M.S., Sroczynski, N., Costelloe, T., Romeijn, R.J., Pastink, A., Mailand, N., Vermeulen, W., and van Attikum, H. (2013). Poly(ADP-ribosyl)ation links the chromatin remodeler SMARCA5/SNF2H to RNF168-dependent DNA damage signaling. J. Cell Sci. *126*, 889–903.

Soutoglou, E., and Misteli, T. (2008). Activation of the cellular DNA damage response in the absence of DNA lesions. Science *320*, 1507–1510.

St Pierre, R., and Kadoch, C. (2017). Mammalian SWI/SNF complexes in cancer: emerging therapeutic opportunities. Curr. Opin. Genet. Dev. *42*, 56–67.

Strickfaden, H., McDonald, D., Kruhlak, M.J., Haince, J.-F., Th'ng, J.P.H., Rouleau, M., Ishibashi, T., Corry, G.N., Ausió, J., Underhill, D.A., et al. (2016). Poly(ADP-ribosyl)ation-dependent transient chromatin decondensation and histone displacement following laser microirradiation. J. Biol. Chem. *291*, 1789–1802.

Timinszky, G., Till, S., Hassa, P.O., Hothorn, M., Kustatscher, G., Nijmeijer, B., Colombelli, J., Altmeyer, M., Stelzer, E.H.K., Scheffzek, K., et al. (2009). A macrodomain-containing histone rearranges chromatin upon sensing PARP1 activation. Nat. Struct. Mol. Biol. *16*, 923–929.

Tulin, A., and Spradling, A. (2003). Chromatin loosening by poly(ADP)-ribose polymerase (PARP) at Drosophila puff loci. Science *299*, 560–562.

Wachsmuth, M., Conrad, C., Bulkescher, J., Koch, B., Mahen, R., Isokane, M., Pepperkok, R., and Ellenberg, J. (2015). High-throughput fluorescence correlation spectroscopy enables analysis of proteome dynamics in living cells. Nat. Biotechnol. *33*, 384–389.

Wollmann, P., Cui, S., Viswanathan, R., Berninghausen, O., Wells, M.N., Moldt, M., Witte, G., Butryn, A., Wendler, P., Beckmann, R., et al. (2011). Structure and mechanism of the Swi2/Snf2 remodeller Mot1 in complex with its substrate TBP. Nature *475*, 403–407.

Wright, R.H.G., Lioutas, A., Le Dily, F., Soronellas, D., Pohl, A., Bonet, J., Nacht, A.S., Samino, S., Font-Mateu, J., Vicent, G.P., et al. (2016). ADP-ribose-derived nuclear ATP synthesis by NUDIX5 is required for chromatin remodeling. Science *352*, 1221–1225.

Yan, L., Wang, L., Tian, Y., Xia, X., and Chen, Z. (2016). Structure and regulation of the chromatin remodeller ISWI. Nature *540*, 466–469.

Zhao, D., Lu, X., Wang, G., Lan, Z., Liao, W., Li, J., Liang, X., Chen, J.R., Shah, S., Shang, X., et al. (2017). Synthetic essentiality of chromatin remodelling factor CHD1 in PTEN-deficient cancer. Nature *542*, 484–488.

Zolghadr, K., Rothbauer, U., and Leonhardt, H. (2012). The fluorescent two-hybrid (F2H) assay for direct analysis of protein-protein interactions in living cells. Methods Mol. Biol. *812*, 275–282.

STAR★METHODS

KEY RESOURCES TABLE

REAGENT or RESOURCE	SOURCE	IDENTIFIER
Antibodies		
Rabbit anti-mCherry-antibody	Novus Bio	NBP2-25157
Bacterial and Virus Strains		
Escherichia coli DH5 alpha	Thermo-Fisher Scientific	18265017
Escherichia coli Rosetta (DE3) pLysS Competent Cells - Novagen	Merck Millipore	70956
Escherichia coli DH10MultiBac	Geneva Biotech	DH10MultiBac
Spodoptera frugipeda Sf21 insect cells	ThermoFisher Scientific (Invitrogen)	11497013
Trichoplusia ni High Five insect cells	ThermoFisher Scientific (Invitrogen)	B85502
Chemicals, Peptides, and Recombinant Proteins		
Immobilized pepsin (agarose resin) for online digestion (HDX-MS)	ThermoFisher Scientific	20343
AG14361	Selleckchem	S2178
Homo bi-functional cross-linker BS3	ProteoChem	c1103
Ammonium bicarbonate (NH4HCO3)	Sigma	09830
DMSO	Life Technologies	D12345
Trypsin	Promega	V511B
Sep-Pak tC18 Cartridges	Waters	WAT043410
PARP1inhibitor AG14361	Selleck Chemicals	S2178
Di- and tri-ADP-ribose	(Kistemaker et al., 2015)	N/A
Adenosine 5′-diphosphoribose (ADPr)	Sigma	A0752
DMEM Dulbecco's	Sigma	S5796
FBS	GIBCO	10270
Sodium pyruvate	Sigma	S8636
L-glutamine	Sigma	G7513
Penicillin	Sigma	P3032
Streptomycin	Sigma	S9137
Hygromycin B	Sigma	H3274
CO_2-independent imaging medium	GIBCO by Life technologies	18045-054
Cell culture Dulbecco's PBS	Sigma	D8537
Critical Commercial Assays		
SYPRO Orange, 5000x in DMSO	Sigma	S5692
Biomol Green	Enzo Life Sciences	BML-AK111
Gel filtration calibraton kit, Low Molecular Weight	GE Healthcare	17-0442-01
Gel filtration standards	BioRad	151-1901
384-well Microplates; ATPase assay	Greiner Bio One	781101
Borosilicate 8-well LabTeks	Thermo-Scientific	155411
X-fect transfection reagent	Clontech	631317
GFP-Trap_A	Chromotek	gta-20
Experimental Models: Cell Lines		
Human U2OS cells harboring the stably integrated lacO (256x) array	(Soutoglou and Misteli, 2008)	N/A

(*Continued on next page*)

Continued

REAGENT or RESOURCE	SOURCE	IDENTIFIER
Recombinant DNA		
pmCherry-C1 Vector	This study	See Table S3
pmCherry-LacI-C1	This study	See Table S3
pmCherry-N1Human SSRP1	This study	See Table S3; digested with XhoI and HindIII and cloned into mCherry-N1 vector
pEYFP-ALC1-1-897-C1	(Gottschalk et al., 2009)	N/A
pmCherry-LacI-ALC1-1-897-C1	This study	See Table S3
pmCherry-LacI-ALC1-1-706-C1	This study	See Table S3
pmCherry-LacI-ALC1-1-673-C1	This study	See Table S3
pmCherry-LacI-ALC1-1-614-C1	This study	See Table S3
pmEGFP-LacI-ALC1-616-897-C1	This study	See Table S3; subcloned from pEYFP-ALC1-1-897-C1 between BglII-EcoR1
pmCherry-LacI-ALC1-616-897-C1	This study	See Table S3; subcloned from pmEGFP-LacI-616-897-C1; BglII and EcoR1
pEYFP-ALC1-1-614-C1	This study	See Table S3
pmEGFP- ALC1-1-897-C1	This study	See Table S3; subcloned from pEYFP-ALC1-1-897-C1 (Restriction sites BglII and ECoR1)
pmEGFP-ALC1-616-897-C1	This study	See Table S3; subcloned from pmEGFP-LacI-616-897-C1; Restriction sites BglII and EcoR1
pET-MCN-ALC1-31-878	This study	See Table S3
pET-MCN-ALC1-31-615	This study	See Table S3
pET-MCN-ALC1-31-605	This study	See Table S3
pET-MCN-ALC1-616-876	This study	See Table S3
pET-MCN-V5-ALC-616-876	This study	See Table S3
pET-MCN-ALC-636-876	This study	See Table S3
pETM-11: ALC1 31-673	This study	See Table S3
pmEGFP-C1Human Spt16	This study	See Table S3
pFBDM-TWINStrep-ALC1-1-897	This study	See Table S3
pcDNA3eYFP-Af1521-macrodomain	(Timinszky et al., 2009)	N/A
pcDNA3eYFP-macroH2A1.1-macrodomain	(Timinszky et al., 2009)	N/A
pcDNA3eYFP-macroH2A1.2-macrodomain	(Timinszky et al., 2009)	N/A
pET-MCN-V5-ALC-616-876: G750E	This study	See Table S3
pmEGFP-ALC1-616-897-C1: G750E	This study	See Table S3
pmEGFP-ALC1-1-897-C1: G750E	This study	See Table S3
pmCherry-LacI-ALC1-1-614-C1: E175Q	This study	See Table S3
pmCherry-LacI-ALC1-1-614-C1: EPEPFE/APAPAA	This study	See Table S3
pmEGFP-ALC1-1-897-C1: EPEPFE/APAPAA	This study	See Table S3
pmCherry-LacI-ALC1-1-614-C1: PEPFE/PAPAA	This study	See Table S3
pmCherry-LacI-ALC1-1-614-C1: RK319/320EE -KR407/422DE	This study	See Table S3
pmCherry-LacI-ALC1-1-614-C1: KR407/422DE	This study	See Table S3
pmCherry-LacI-ALC1-1-614-C1: KK307/ 308EE-K398E	This study	See Table S3
pmCherry-LacI-ALC1-1-614-C1: S420A	This study	See Table S3
pmEGFP-ALC1-616-897-C1: 653-KRRR-656/ AAAA-G750E	This study	See Table S3
pmEGFP-ALC1-616-897-C1: R857E/G750E	This study	See Table S3
pmEGFP-ALC1-616-897-C1: R857Q/G750E	This study	See Table S3
pmEGFP-ALC1-1-897-C1: R857Q	This study	See Table S3

(*Continued on next page*)

Continued

REAGENT or RESOURCE	SOURCE	IDENTIFIER
pmEGFP-ALC1-616-897-C1: R842H/ R860W/G750E	This study	See Table S3
pmEGFP-ALC1-1-897-C1: R842H/R860W	This study	See Table S3
pmEGFP-ALC1-1-897-C1: R842H	This study	See Table S3
pmEGFP-ALC1-1-897-C1: R860W	This study	See Table S3
Software and Algorithms		
ProteinLynx Global Server 3.0	http://www.waters.com/waters/home.htm (Waters)	N/A
DynamX 3.0	http://www.waters.com/waters/home.htm (Waters)	N/A
MS Convert Proteowizard Tools	http://proteowizard.sourceforge.net/tools.shtml	N/A
Crossfinder	(Mueller-Planitz, 2015)	N/A
PEAQ-ITC Analysis Software	https://www.malvern.com/en/ (Malvern)	N/A
Graphpad-Prism	https://www.graphpad.com/scientific-software/prism/	N/A
FIJI(ImageJ)	(Schindelin et al., 2012)	N/A
Fluctuation Analyzer 4G software	(Wachsmuth et al., 2015)	N/A
Other		
Superdex 200 Increase 10/300 GL	GE Healthcare	28990944
15-cm analytical column C18 nanocolumn (75 μm ID homepacked with ReproSil-Pur C18-AQ 2.4 μm)	N/A	N/A
Ultimate 3000 HPLC system	ThermoFisher Scientific	IQLAAAGABHFAPBMBFB

CONTACT FOR REAGENT AND RESOURCE SHARING

Further information and requests for resources and reagents should be directed to and will be fulfilled by the Lead Contact, Andreas G. Ladurner (andreas.ladurner@bmc.med.lmu.de).

METHOD DETAILS

Cloning, protein expression and purification

All human ALC1 fragments and mutants were engineered by sub-cloning and site-directed mutagenesis, using oligonucleotides defined in Table S3. Recombinant proteins were expressed and purified as N-terminally 6 × His-tagged fusion proteins from *E. coli* Rosetta (DE3) pLys using pETM-CN or pETM-11 (only for ALC1 31-674) vectors. Starting cultures were grown in LB-medium supplemented with the appropriate antibiotics over night at 30°C and used at a 1:50 dilution to inoculate the expression cultures. Expression cultures were then grown in rich medium (supplemented with antibiotics) at 37°C and 160-200 rpm until reaching an OD_{600} of 0.6 – 0.8 before protein expression was induced with 0.2 mM isopropyl β-D-1 thiogalactopyranoside (IPTG). After induction, protein expression was allowed to proceed for 18 hr at 18°C (ALC1 570-897, 31-605, 31-615, 615-876, V5-615-876, 636-878) or 16°C (ALC1 31-674, 3-897, 31-878) until the cells were harvested by centrifugation at 8,000 × *g* for 10 min. Bacterial pellets were either directly used for protein purification or stored at −80°C. The cells were lysed by sonication at 4°C in lysis buffer (50 mM Tris-HCl pH 7.5, 500 mM NaCl, 20 mM imidazole, 5 mM dithiothreitol (DTT) and Complete EDTA free protease inhibitor tablets (Roche). The lysate was cleared by centrifugation at 45,000 × g and loaded onto Ni-Sepharose 6FF beads for batch purifications or a HisTrap HP 1mL column operated on a ÄKTA pure FPLC system (GE Healthcare). After washing with several (15-30) column volumes (CV) lysis buffer, proteins were eluted either stepwise (batch purification) or in a 15 CV gradient of elution buffer (lysis buffer supplemented with 500 mM imidazole). The eluate was concentrated by ultrafiltration (Vivaspin 30,000 MWCO, Sartorius) and loaded onto a Superdex 200 16/60 column (GE Healthcare) equilibrated in SEC-buffer (25 mM Tris-HCl pH 7.5, 200 mM NaCl, 1 mM DTT). Peak fractions were pooled and diluted with dilution buffer (25 mM Tris-HCl pH 7.5, 2 mM DTT) to a final salt concentration of 50 mM NaCl (low-salt buffer) and loaded onto a cation exchange column (MonoS 5/5 HR or Resource S 6mL (GE Healthcare), full length and Macro domain constructs), or an anion exchange column (MonoQ 5/5 HR or Resource Q 6mL (GE Healthcare), ATPase constructs) pre-equilibrated with low-salt buffer. After washing with 5-10 CV low-salt buffer, proteins were eluted by increasing the NaCl concentrations to

500 mM in a linear gradient of 10-20 CV. Peak fractions were again pooled and concentrated by ultrafiltration (Vivaspin 30,000 MWCO, Sartorius). The purified proteins were either used directly or snap-frozen in liquid nitrogen for storage at −80°C. For the ITC assays, the macrodomain of macroH2A1.1 was expressed and purified, as published (Kustatscher et al., 2005; Timinszky et al., 2009). Briefly, N-terminally 6 × His-tagged of MacroH2A1.1 (residues 162-369) was expressed for 3 hr at 37°C after induction with 1 mM IPTG. The cells were lysed in 50 mM Tris-HCl pH 7.4, 500 mM NaCl, 1 mM MgCl2, 5 mM β-ME and 10% (v/v) glycerol. The protein was bound to Ni-Sepharose 6FF beads, washed with lysis buffer containing 1 M NaCl and 40 mM imidazole, and eluted in lysis buffer supplemented with 500 mM imidazole. The ALC1 macrodomain and the ALC1 ATPase module were purified as described above.

Limited trypsin proteolysis

500 μl of purified Hs ALC1 (3-897; full-length) or Hs ALC1 (570-897; macrodomain) at a concentration of 1 mg/ml were incubated at room temperature (RT) with trypsin (Sigma Aldrich) at a ratio of 1:100 (full-length) and 1:10 (macrodomain). Reactions were stopped by addition of protein gel loading buffer and boiling (for SDS-PAGE analysis) or 2 mM PMSF (final; for analytical SEC analysis). The resulting major bands on the SDS-PAGE gels were used for MALDI peptide mass fingerprinting to identify the peptides corresponding the particular band.

Full-length ALC1 baculovirus cloning expression and purification

Full length human ALC1 (1-897) was expressed as N-terminally Twin-Strep-tagged fusion protein using MultiBac technology (Fitzgerald et al., 2006). Briefly, cDNA was cloned into pFBDM vector for expression under control of a polyhedrin promotor. Transposition into MultiBac baculoviral DNA was performed in E. coli DH10MultiBac cells (Geneva Biotech). Isolated bacmid DNA was transfected into *Spodoptera frugipeda* Sf21 insect cells (Invitrogen) in order to generate baculovirus, while large-scale protein expression was carried out using *Trichoplusia ni* High Five insect cells (Invitrogen). High Five cells were infected with 1/100 (v/v) with baculovirus. Cells were cultured for 60 hr at 27°C until they were harvested by centrifugation. Cells were lysed by gentle sonication in lysis buffer (20 mM HEPES pH 8.0, 500 mM NaCl, 10% [v/v] Glycerol, 2 mM MgCl2, 1 mM DTT) and complete EDTA free protease inhibitor tablets (Roche). The lysate was cleared by centrifugation and loaded onto Streptactin-Sepharose (IBA) for batch purification. After washing beads with lysis buffer, protein was eluted using 3.5 mM d-Desthiobiotin (Sigma). The eluate was concentrated by ultrafiltration (Vivaspin 30,000 MWCO, Sartorius) and loaded onto a Superdex 200 16/60 column (GE Healthcare) equilibrated in SEC-buffer (20 mM HEPES pH 8.0, 500 mM NaCl, 10% [v/v] Glycerol, 2 mM MgCl2, 1 mM DTT). Purified, monodisperse ALC1 protein was snap-frozen in liquid nitrogen for storage at −80°C.

Hydrogen deuterium exchange mass-spectrometry (HDX-MS)

For HDX labeling: All proteins were incubated for 30 min at 25°C before initiating the labeling reactions. Deuterated buffer (2.5 mM Tris (pH 7.5), 150 mM NaCl, 0.1 mM DTT) was added in a 10:1 dilution (v/v), resulting in 90% (v/v) D_2O and 0.8 μM protein concentration during labeling. The reactions were incubated for various time intervals ranging from 0.25 to 60 min. The following labeling reactions were prepared in duplicates unless otherwise specified: a) A full time series of the full length ALC1 with and without 5-fold molar excess of tri-ADP-ribose. Single measurements were conducted for the entire time series and from the results, two time points (0.25 and 10 min) were selected for triplicate measurements. b) A 10 min time point of the full length ALC1 with and without 50-fold molar excess of tri-ADP-ribose. c) A 0.25 min time point of the Macrodomain with and without 5-fold molar excess of tri-ADP-ribose or 50-fold molar excess of mono-ADP-ribose). d) A 0.25 min time point of the 1:1 molar ratio mixture of the ATPase domain and the Macrodomain with and without 5-fold molar excess of tri-ADP-ribose. Following the indicated incubation periods, the labeling reactions were quenched by 1:1 (v/v) dilution into ice-cold quench buffer (219 mM potassium phosphate (pH 2.5), 6 M urea). The quenched samples were immediately frozen and stored at −80°C. For LC-MS and LC-MS/MS measurements: Samples were quickly thawed and injected into a Waters nanoAcquity UPLC system with an HDX Manager which allows for online digestion at 20°C and desalting and separation of peptides at 0°C. Following online digestion on column packed with immobilized pepsin on agarose (Thermo Scientific Pierce, Rockford, USA), the peptic peptides were trapped on a C18 Vanguard trap column (Acquity UPLC BEH C18 column, 130Å, 1.7 μm, 2.1mm X 5 mm – Waters – Product number: 186003975) and desalted for 3 min with 0.23% formic acid in water (pH 2.5) at a flow rate of 200 μl/min. The peptides were eluted from the trap column to an analytical column (Acquity UPLC BEH C18 column, 130Å, 1.7 μm, 1mm X 100 mm – Waters – Product number: 186002346) fitted with a C18 Vanguard column (Acquity UPLC BEH C18 column, 130Å, 1.7 μm, 2.1mm X 5 mm – Waters – Product number: 186003975) and separated using a 9 min gradient from 8% to 40% of 0.23% formic acid in acetonitrile at a flow rate of 40 μl/min. The peptides were ionized by electrospray ionization and mass spectra collected using a Waters Synapt G2 HDMS mass spectrometer set in positive ion mode. Peptic peptides of non-deuteriated samples were identified in a separate experiment using collision-induced dissociation tandem mass spectrometry with data collected in a data-independent (MS^E) manner. Peptide identification was carried out using ProteinLynx Global Server 3.0 and the HDX-MS data was processed using DynamX 3.0 from Waters.

Chemical cross-linking coupled to mass spectrometry (XL-MS)

Cross-linking reactions were carried out with 1 μM purified ALC1 full-length protein in 25mM HEPES KOH pH 7.6, 0.1 mM EDTA, 10% glycerol, 100 mM KOAc, 1.5 mM MgCl2, 1 mM DTT. The homobifunctional cross-linker BS3 (ProteoChem) was dissolved freshly in

DMSO and added to a final concentration of 1 mM. The cross-linking reactions and a mock-treated control were incubated on ice for 20 min before quenching with NH_4HCO_3 to a final concentration of 200 mM for 10 min. The protein sample was loaded onto a pre-equilibrated Superdex 200 (Increase 10/300 GL, GE Healthcare). The elution profile at 280 nm was consistent with ALC1 being monomeric in solution and no evidence for a possible dimer formation was observed. Protein fractions were pooled and concentrated by the addition of 15% (w/v) trichloroacetic acid with pelleting. The pellet was washed twice with acetone and re-dissolved in 8 M urea. In-solution digestion was performed after urea dilution with trypsin (enzyme to substrate ratio 1:50) at 37°C overnight. Digestion was stopped by the addition of 2% (v/v) formic acid. Acidified peptides were purified and concentrated by a C18 resin (Sep-Pak tC18 Cartridges, Waters). The eluate was dried by vacuum centrifugation and re-dissolved in 0.1% trifluoroacetic acid. To map the cross-links by LC-MS/MS, samples were desalted offline using C18 Stagetip and injected in an Ultimate 3000 (Thermo) or RSLCnano system (Thermo). Peptides were separated in a 15 cm analytical column C18 nanocolumn (75 μm ID homepacked with ReproSil-Pur C18-AQ 2.4 μm from Dr. Maisch) with a 40 or 60 min gradient from 5 to 60% acetonitrile in 0.1% formic acid. The effluent from the HPLC was directly electrosprayed into a Q Exactive HF (Thermo). The Q Exactive HF instrument was operated in data dependent mode to automatically switch between full scan MS and MS/MS acquisition. Survey full scan MS spectra (from m/z 375–1600) were acquired with resolution R = 60,000 at m/z 400 (AGC target of 3x106). The ten most intense peptide ions with charge states between 3 and 5 were sequentially isolated to a target value of $1x10^5$, and fragmented at 27% normalized collision energy. Typical mass spectrometric conditions were: spray voltage, 1.5 kV; no sheath and auxiliary gas flow; heated capillary temperature, 250°C; ion selection threshold, 33.000 counts. Thermo binary raw file were transformed to mzXML files using msconvert (Proteowizard Tools; proteowizard.sourceforge.net/tools.shtml). Cross-linked peptides were identified using Crossfinder (Mueller-Planitz, 2015). An MS1 and MS2 tolerance window of 10 and 12 ppm, respectively, was applied. The number of missed trypsin cleavage sites was set to three. For all peptides, oxidation of methionine was set as variable modification and carbamido methylation as fixed modification. All lysine residues were considered as potential cross-linking sites for BS3. False-discovery rates (FDRs) were estimated by Crossfinder and results were filtered according the following parameters for identification of cross-linking candidates: FDR < 1%, number of fragment ions per spectrum ≥ 6, number of fragment ions per peptide ≥ 3, number of fragment ions with cross-linker ≥ 1, fractional intensity of assigned MS2 peaks ≥ 0.05, relative filter score: 100. We ensured that cross-linking candidates were not present in the mock-treated sample. MS2 spectra of cross-linking candidates spanning at least 10 amino acids in the primary sequence were manually validated.

Isothermal titration calorimetry (ITC) assays

For ITC binding assays the Peaq-ITC instrument (Malvern) was used. Before the experiment, proteins were dialyzed overnight against 25 mM Tris, 100 mM NaCl buffer (pH 7.5) and 5 mM 2-mercaptoethanol at 4°C. The dialyzed proteins were then centrifuged for 20 min at 35,000 g at 4°C and the protein concentration was determined by absorbance measurements at 280 nm wavelength using calculated molar extinction coefficients. All the ITC experiments were carried out at 25°C. The binding reactions were performed using 5-15 μM macrodomain and 50-150 μM ligand in the syringe. For the ALC1 macrodomain–ATPase interaction studies, all the experiments were carried out using 10 μM ATPase (cell) and 120 μM of ALC1 macrodomain (syringe). For the competition assay, 4.5 μM ALC1 macrodomain was incubated with 2-fold molar excess of tri-ADP ribose (9 μM) at room temperature and then loaded into the cell. The same molar concentration of tri-ADP ribose was added into the ligand-containing solution consisting of 45 μM of ATPase. PEAQ-ITC Analysis Software (Malvern) was used for data analysis. GraphPad Prism software was used to plot the data. Adenosine 5′-diphosphoribose was bought from Sigma (A0752). Di- and tri-ADP ribose were synthetized and purified (Kistemaker et al., 2015).

Plasmids for cellular assays

The mammalian expression constructs of N-terminally fluorescent tagged bait and prey were generated by cloning of the relevant DNA sequences in the fluorescently tagged LacR containing mammalian expression vectors and without LacR containing mammalian expression vectors, respectively (Table S3). All plasmids were generated following usual cloning procedure and were validated by Sanger sequencing.

Cell culture and transfections

For all the F2H assays, human U2OS cells harboring the stably integrated lacO (256x) array was used (Soutoglou and Misteli, 2008). Cells were cultured in DMEM (Sigma) supplemented with 10% (v/v) FBS (GIBCO), 1 mM sodium pyruvate (Sigma), 2 mM L-glutamine (Sigma), 100 U ml^{-1} penicillin, 100 mg ml^{-1} streptomycin (Sigma) and 200 mg ml^{-1} hygromycin B (Sigma) with 5% CO2 at 37°C in a humidified environment.

Microscopy experiments

All microscopy experiments were performed in borosilicate 8-well Lab-Teks (Thermo Scientific). A Zeiss AxioObserver Z1 confocal spinning disk microscope was used for imaging. Images were acquired with an AxioCam HRm CCD /EMCCD/cCMOS camera (Zeiss) using Zeiss C-Apochromat 40x/1.2 water immersion and 63x/oil immersion objective lenses. Cells were imaged 24 hr post-transfection.

UV-laser micro-irradiation assays

Live cells were imaged on a AxioObserver Z1 confocal spinning-disk microscope equipped with an AxioCam HRm CCD camera (Zeiss) through a Zeiss 40x/water objective lens. For laser micro-irradiation, a 355-nm-wavelength diode-pumped solid-state pulsed laser (DPSL-355/14, Rapp OptoElectronics) was used. DNA damage was induced by focusing the 355 nm pulsed laser in the nucleus either as a small circle or as a line through the entire diameter of the nucleus. Cells were imaged at room temperature in a CO_2 independent medium (1x; GIBCO).

PARP1 inhibitor treatment and H_2O_2 treatments

For F2H and laser micro-irradiation experiments, cells were treated with 30 μM of the PARP1 inhibitor AG14361 (Selleck Chemicals) for at least 60 min, for the LacO array de-compaction experiments with PARP1 inhibitor cells were treated with the inhibitor for at least 24 hr before imaging (at the time of transfection itself). Cells were imaged immediately after H_2O_2 treatment, which was diluted to 1:2000 from stock H_2O_2 solution (30% v/v) in the imaging medium.

Fluorescence two-hybrid (F2H) assay

F2H assays were performed as previously described (Bowman et al., 2016; Czarna et al., 2013). Briefly, assays were performed in borosilicate 8-well Lab-Teks (Thermo Scientific). The fluorescently tagged bait and prey proteins were transiently co-transfected, using Xfect reagent (Clontech) according to the manufacturer's recommendations. Cells were imaged at 25°C in a CO2-independent imaging medium (GIBCO) supplemented with 10% (v/v) FBS (GIBCO), 1 mM Sodium pyruvate (Sigma), 2 mM L-glutamine (Sigma), 100 U ml^{-1} penicillin, 100 mg ml^{-1} streptomycin (Sigma). Image analysis was manually performed with FIJI (ImageJ) image analysis software (Schindelin et al., 2012). Briefly, the average fluorescence intensity of the prey (mEGFP fusion) over the LacO array was divided by the average fluorescence intensity in the nucleoplasm to get the enrichment ratio. The fluorescent bait spot was identified by the localization of anchored bait protein (Fluorescent LacI fusion) on the LacO array. Only the cells that show a clearly discernible Lac repressor spot in the nuclei were chosen for analysis. The fluorescence intensity of the prey on the array and outside the array (nucleoplasm) was calculated, background subtracted and plotted as the ratio of the two (as enrichment ratio).

Co-immunoprecipitation assays

To test whether ALC1 oligomerizes *in vivo*, EGFP- and mCherry-tagged ALC1, EGFP-SPT16 and SSRP1-mCherry (positive control) or EGFP and mCherry-ALC1 (negative control) were expressed in U2OS cells for 24 hr and treated with 30 μM AG14361 PARP Inhibitor (Selleckchem) for 1 hr before lysis. GFP-tagged proteins were immunoprecipitated using GFP-trap (Chromotek) following manufacturer's instructions. AG14361 (30 μM) was further supplied during all incubation steps. Interaction between GFP- and mCherry-tagged proteins was examined by western blotting using GFP- (Eurogentec) and mCherry-antibodies (Novus Bio, NBP2-25157), respectively.

LacO array remodelling assays

The LacO array de-compaction assays was performed in the same way as the F2H assay, with the only difference in the analysis of the results, wherein the area covered by the Lac repressor fusion protein on the LacO array was measured and normalized by the total area of the same nuclei, which was then plotted as % Nucleus area. Only the cells, which show a clearly discernible Lac Repressor decompacted spot in the nuclei, were chosen for analysis.

V5-Macrodomain pull-down assays

For V5-Macrodomain pull-down assays V5-tagged Macrodomain (615-876) of ALC1 was used as bait on the anti-V5 Agarose affinity gel beads in 1x PBS buffer. Other indicated proteins (like ATPase domain, PARP1) and ligands (DNA, NAD^+, ADP-ribose ligands, PolyA-DNA, PARP1 inhibitor) were added to the pre-incubated V5-macrodomain bound beads as indicted and the complex was incubated on room temperature for 30 min before centrifugation followed by 3 washes in PBS and was finally boiled in Laemmli buffer before running on a 4%–12% gradient SDS-PAGE gel.

Fluorescence correlation spectroscopy (FCS)

FCS experiments were performed on a Leica SP8 confocal microscope equipped with a Plan APO 63x/1.2 N.A. water immersion objective. GFP fluorescence was excited with a 488 nm laser and emission selected by a bandpass filter at 500-550 nm. Laser power used for FCS measurements was adjusted to minimize photobleaching. Pinhole was set to one Airy unit. Single photons were detected and counted using a single photon avalanche diode and a PicoHarp module from PicoQuant. To estimate the residence time of GFP-tagged constructs in the focal volume, autocorrelation curves were fitted with a one-species model assuming pure diffusion and neglecting the contribution of the photo-physics of GFP using the Fluctuation Analyzer 4G software (Wachsmuth et al., 2015).

Thermal shift assays

Fluorescence-based thermal shift assays were conducted on an Applied Biosystems 7500 fast real-time PCR system. 2 μM protein solutions supplemented with 5 × SYPRO Orange in the absence or presence of 6.5μM tri-ADP-ribose or 19.5μM ADP-ribose were

heated in 25mM Na-PO_4 (pH 7.0), 0.25M NaCl and 1mM DTT from 5°C to 95°C at a ramp rate of 1%. The assays were conducted in MicroAmp Fast 96-well reaction plates sealed with MicroAmp Optical Adhesive Film (Applied Biosystems). The fluorescence measurements at 554nm were normalized to the lowest value before the transition and the maximum fluorescence.

Chromatin remodeler ATPase assays

The ALC1 catalyzed ATP hydrolysis was performed in 384-well using a malachite green assay (Greiner Bio One). For this, 1μM recombinant (near) full length ALC1 protein (residues 31-878) or the constitutively active ATPase fragment (residues 31-674) were pre-incubated for 10 min at RT with 1 μM dsDNA (75 bp with 4 nt overhangs on both ends; see Key Resources Table for their sequence) in 25 mM Bis-Tris pH 7.0, 0.15 M NaCl, 1 mM $MgCl_2$, 50 μM $ZnCl_2$, 1 mM DTT and 5% (w/v) glycerol in the absence or presence of ligand (5 μM tri-ADP-ribose or 15μM monomeric ADP-ribose). In case of the constitutively active ATPase fragment, the reactions were additionally performed in the absence or presence of 2.5μM ALC1 macrodomain (residues 636-878). The reactions were started by the addition of 1 μL 1 mM ATP, giving a final volume of 10 μL. After 5 min at RT, the reactions were stopped by the addition of 20 μL Biomol Green (Enzo Life Sciences), and the color was allowed to develop for 15 min. The absorbance of the resulting phosphomolybdate complex was read at 640 nm on a Tecan Infinite M1000 Pro microplate reader.

Analytical size exclusion chromatography (aSEC)

Globular proteins of known molecular weight from the Gel Filtration Calibration kit (GE Healthcare) and a Gel Filtration Standard (BioRad) were used to calibrate a Superdex 200 Increase 10/300 column (GE Healthcare). Blue dextran was used to determine the column void volume. Protein elution volumes were measured by monitoring the absorption at 280 nm. The elution volumes were used to calculate the partition coefficient (K_{av}) with the formula $K_{av} = (V_e - V_0)/(V_t - V_0)$ where V_e is the elution volume, V_0 is the void volume, and V_t is the total volume of the column. The apparent molecular weight was then derived from the inverse logarithm of the partition coefficient. All aSEC experiments were performed in 25 mM Na-PO_4 (pH 7.0), 0.25 M NaCl and 1 mM DTT.

QUANTIFICATION AND STATISTICAL ANALYSIS

For *in vitro* ATPase and Thermofluor assays

The experiments were performed three times as technical triplicates. The blank-subtracted values were normalized to the respective mean ATPase activity in the absence of the macrodomain or to the mean activity of the full-length protein. Blank values were determined by measuring the absorbance under identical conditions without ATP. All Thermofluor experiments were performed multiple times as technical replicates.

For the F2H and lacO array assays

The Wilcoxon matched-pairs signed rank test was used since normal distribution could not be assumed to determine the statistical significance in F2H and LacO decompaction assays (biological replicates $n \geq 2$). The column in the graph represents the *Mean*, error bar represents the SEM and number of cells is ≥ 20. Actual p values are indicated in the figures. GraphPad Prism software was used to plot and analyze the data.

For HDX-MS measurements

For statistical analysis of the HDX-MS data, the standard deviation of measured deuterium content in each peptide based on technical replicates (n = 2 or n = 3) and using all relevant charge states. A significance threshold for differences in HDX between individual protein states was set to 0.52 D, corresponding to the 98.75% confidence interval (CI) calculated using technical replicates (n = 3) data from a single time-point for full-length ALC1 in the presence or absence of tri-ADP-ribose. The CI was calculated according to:

$$CI = \overline{x} \pm t * \frac{\sigma}{\sqrt{n}}$$

where x is the average difference in deuterium content assuming a zero-centered distribution ($x = 0$), t is 8.86 for the 98.75% CI with 2 degrees of freedom, σ is the average propagated standard deviation of differences in deuterium content for all peptide segments, and n is the number of replicate samples (n = 3).